Article

Immunity

Interplay between liver and blood stages of *Plasmodium* infection dictates malaria severity via γδ T cells and IL-17-promoted stress erythropoiesis

Graphical abstract

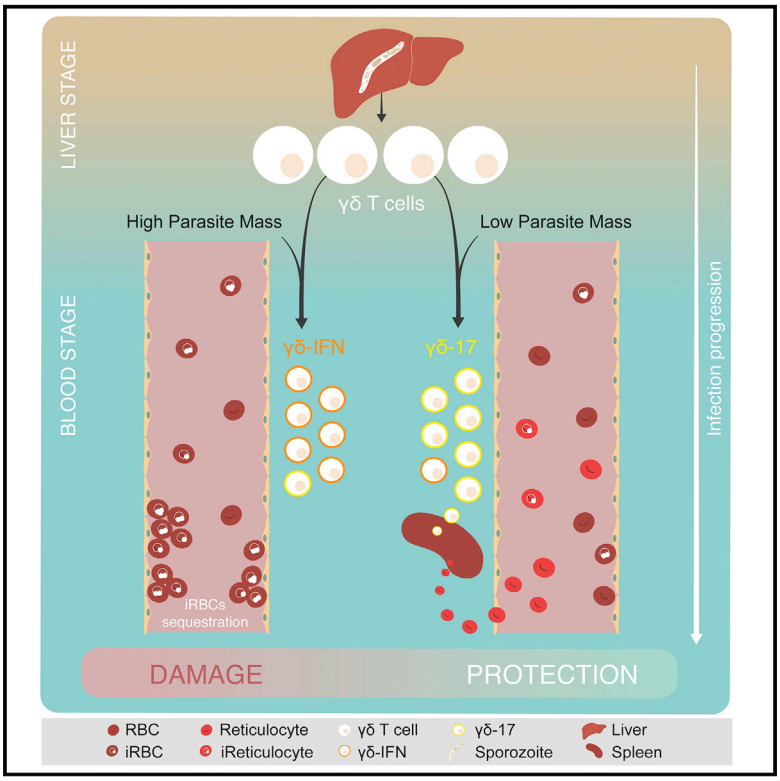

Authors

Ângelo Ferreira Chora, Sofia Marques, Joana Lisboa Gonçalves, ..., Bruno Silva-Santos, Ann T. Tate, Maria M. Mota

Correspondence

angelochora@medicina.ulisboa.pt (Â.F.C.), mmota@medicina.ulisboa.pt (M.M.M.)

In brief

The impact of liver stage *Plasmodium* infection on clinical outcomes of malaria is underappreciated. Chora et al. demonstrate an important role in liver stage-dependent activation of γδ T cells and further show that the integration of host responses during both liver and blood stages of infection dictates malaria severity.

Highlights

- The liver stage of *Plasmodium* infection impacts the clinical outcome of malaria
- The outcome of infection relies on the liver stage activation of distinct γδ T cell subsets
- γδ T cells and IL-17 promote splenic erythropoiesis and reticulocytosis
- Increased reticulocyte availability curtails the development of ECM

Chora et al., 2023, Immunity *56*, 592–605
March 14, 2023
https://doi.org/10.1016/j.immuni.2023.01.031

CellPress

CellPress
OPEN ACCESS

Immunity

Article

Interplay between liver and blood stages of *Plasmodium* infection dictates malaria severity via γδ T cells and IL-17-promoted stress erythropoiesis

Ângelo Ferreira Chora,[1,*] Sofia Marques,[1] Joana Lisboa Gonçalves,[1] Priscila Lima,[1] Daniel Gomes da Costa,[1] Daniel Fernandez-Ruiz,[2] Maria Inês Marreiros,[1] Pedro Ruivo,[1] Tânia Carvalho,[1] Ruy M. Ribeiro,[3] Karine Serre,[1] William R. Heath,[2,4] Bruno Silva-Santos,[1] Ann T. Tate,[5] and Maria M. Mota[1,6,*]

[1]Instituto de Medicina Molecular João Lobo Antunes, Faculdade de Medicina da Universidade de Lisboa, 1649-028 Lisboa, Portugal
[2]Department of Microbiology and Immunology, Peter Doherty Institute for Infection and Immunity, University of Melbourne, Melbourne, VIC 3000, Australia
[3]Theoretical Biology and Biophysics, Los Alamos National Laboratory, Los Alamos, NM 87545, USA
[4]ARC Centre of Excellence in Advanced Molecular Imaging, University of Melbourne, Parkville, VIC 3010, Australia
[5]Department of Biological Sciences, Vanderbilt University, Nashville, TN 37232, USA
[6]Lead contact
*Correspondence: angelochora@medicina.ulisboa.pt (Â.F.C.), mmota@medicina.ulisboa.pt (M.M.M.)
https://doi.org/10.1016/j.immuni.2023.01.031

SUMMARY

Plasmodium replicates within the liver prior to reaching the bloodstream and infecting red blood cells. Because clinical manifestations of malaria only arise during the blood stage of infection, a perception exists that liver infection does not impact disease pathology. By developing a murine model where the liver and blood stages of infection are uncoupled, we showed that the integration of signals from both stages dictated mortality outcomes. This dichotomy relied on liver stage-dependent activation of Vγ4$^+$ γδ T cells. Subsequent blood stage parasite loads dictated their cytokine profiles, where low parasite loads preferentially expanded IL-17-producing γδ T cells. IL-17 drove extra-medullary erythropoiesis and concomitant reticulocytosis, which protected mice from lethal experimental cerebral malaria (ECM). Adoptive transfer of erythroid precursors could rescue mice from ECM. Modeling of γδ T cell dynamics suggests that this protective mechanism may be key for the establishment of naturally acquired malaria immunity among frequently exposed individuals.

INTRODUCTION

In malaria-endemic areas, naturally acquired immunity to malaria protects millions of individuals routinely exposed to *Plasmodium falciparum* and other *Plasmodium spp.* parasites against life-threatening manifestations of the disease. The nature of acquired immunity against malaria is, most certainly, multifactorial. Although cumulative exposure to natural *Plasmodium* infections results in decreased levels of circulating parasites, the major readout of acquired immunity to malaria is protection from severe disease and death. Although the establishment of such protective responses has been extensively explored, no single molecular signature, key cellular determinant, or immune mechanism is causally associated with clinical protection from severe malarial disease.[1]

Under natural transmission settings, malaria infections start with the transmission of *Plasmodium* hepatotropic sporozoites (spz) by an infected *Anopheles* mosquito. Once inside hepatocytes, spz replicate into thousands of blood-infectious merozoites, initiating the symptomatic stage of the disease. Indeed, all the clinical symptoms of malaria are a consequence of infection of human erythrocytes.[2] As such, basic research addressing parasite virulence or malaria-associated pathophysiology mostly employs either *in vitro* culture systems of *P. falciparum* in human red blood cells (RBCs) or rodent models of infection initiated by infected (i) RBC transfusion. Both of these experimental strategies ignore the liver stage (LS) of infection altogether, which is assumed to not contribute to the establishment of pathology.[2] However, the LS of infection—traditionally thought to be immunologically silent—can control parasite load by stimulating an innate immune response.[3,4] The host's ability to sense and respond to intra-hepatic parasite forms led us to hypothesize that the LS pre-conditions the host response to the subsequent blood stage (BS) of infection and potentially influences the course of infection. Our data show that, even though severe manifestations of malaria only occur during the BS of infection, signals from the preceding liver stage contribute to disease outcomes. Such crosstalk between parasite developmental stages results in the activation of distinct subsets of γδ T cells, with IL-17-promoted stress erythropoiesis being at the basis of disease protection.

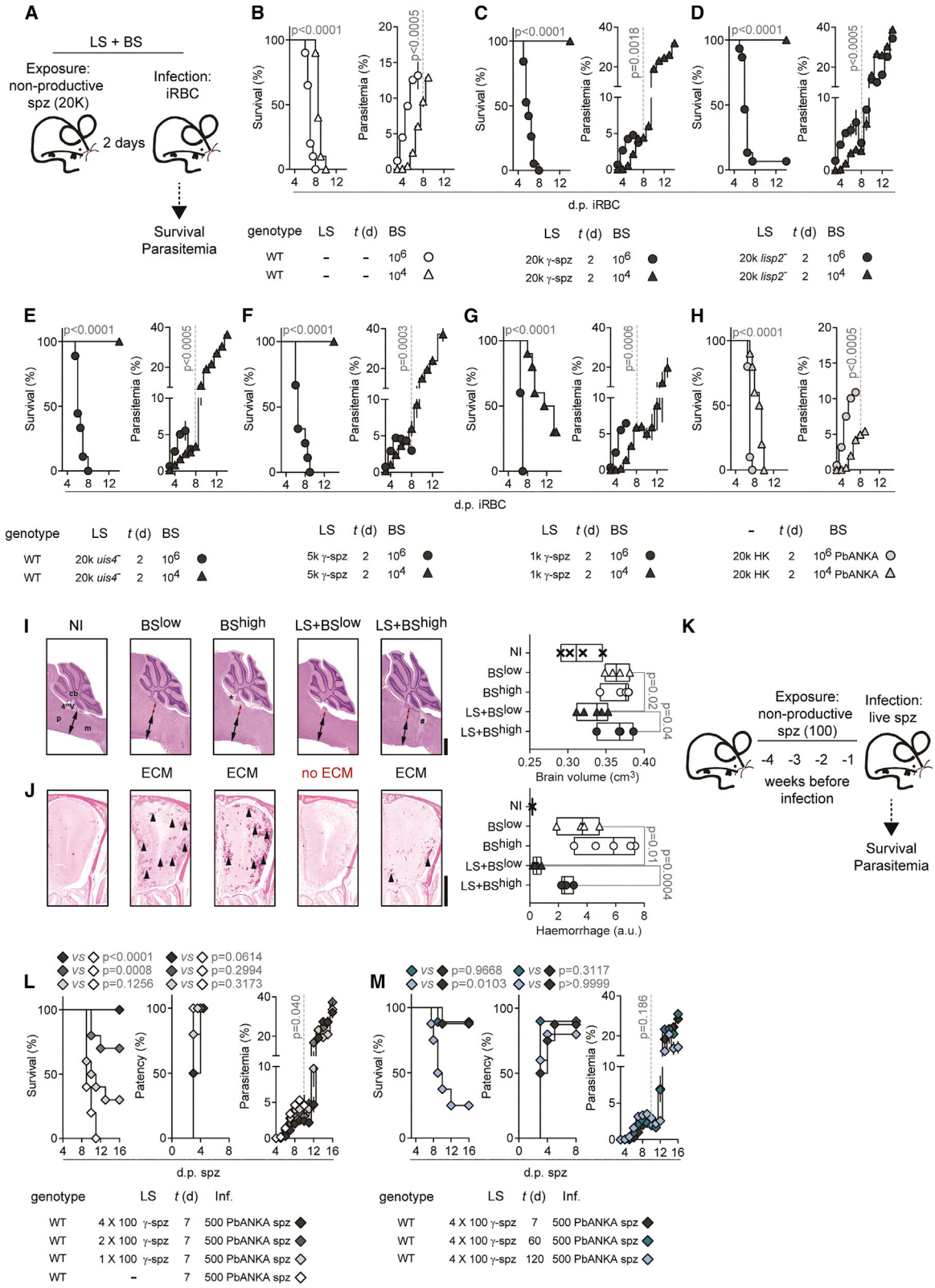

(legend on next page)

RESULTS

Plasmodium cross-stage interplay determines the outcome of malaria

We sought to determine whether the LS contributes to the clinical outcome of *Plasmodium* infections by comparing the course of a BS infection following, or not, an LS infection. However, a direct comparison between spz- and iRBC-initiated infections is challenging as (1) it is difficult to ensure that LS-derived merozoites initiate a BS infection, in both timing and parasite load, comparable with that of an iRBC transfusion and (2) *Plasmodium* passage through the mosquito vector resets parasite virulence via epigenetic reprogramming.[5] To curtail these hurdles, we developed an infection system that enables the uncoupling of the two stages of *Plasmodium* infection within the mammalian host while controlling for the initial BS parasite inoculum. In this system (hereafter termed LS + BS), mice were initially subjected to a non-productive *Plasmodium berghei* ANKA (PbANKA) LS infection, initiated by the administration of attenuated liver-infectious spz that establish within the hepatocyte but do not produce RBC-infective progeny. Two days later, when the egress of LS-produced merossomes and merozoite release starts in rodents infected with virulent spz,[4] a BS infection was initiated by the transfusion of PbANKA iRBCs (Figure 1A). Given that clinical immunity is associated with low parasite load during the erythrocytic stage of parasite development,[6,7] we employed two distinct inocula of iRBC, i.e., 10^4 and 10^6 iRBCs (BS^{low} and BS^{high} infections, respectively). As reported,[8] mice receiving salivary gland material of non-infected (NI) mosquitoes (liver-mocked infection) followed by a BS infection 2 days later succumbed to the neurologic syndrome known as experimental cerebral malaria (ECM), irrespective of the BS inoculum (Figure 1B). LS + BS infections resulted in opposing outcomes, i.e., survival or death, depending on the dose of the iRBC inoculum employed. When subjected to an LS infection (initiated by either a single bolus of 20,000 radiation- or genetically attenuated spz) followed by the inoculation of 10^4 iRBCs (LS + BS^{low}) all mice survived, in contrast to those receiving 10^6 iRBCs (LS + BS^{high}) (Figures 1C–1E). LS infection with a single bolus of 4-fold fewer spz still afforded complete protection following an LS + BS^{low} infection, whereas a 20-fold reduction in LS parasite burden decreased survival by 70% ± 14.1% (Figures 1F and 1G). Protection upon LS + BS^{low} infection was also lost when mice received equivalent amounts of heat-killed spz, implying that such protection requires parasite establishment within hepatocytes (Figure 1H). Histopathological analysis of the central nervous system (CNS) revealed that protected mice receiving an LS + BS^{low} infection showed reduced brain swelling and minimal hemorrhage when compared with either LS + BS^{high}- or BS^{low}-infected mice ($p = 0.0467$ and $p = 0.0004$ vs. LS + BS^{high} and $p = 0.0207$ and $p = 0.015$ vs. BS^{low}, respectively) (Figures 1I and 1J). Akin to ECM (Figures 1B and 1C), the observed protection could be extended to a distinct model of severe disease, malaria-associated acute respiratory distress syndrome (MA-ARDS).[9] Mice exposed to LS + BS^{high}, BS^{high} or BS^{low} infections upon transfusion of iRBCs with the lung-sequestering *P. berghei* K173 (PbK173) strain[10] succumbed to MA-ARDS (Figures S1A and S1B) after developing pulmonary edema and pleural effusion in the absence of overt CNS pathology (Figures S1C–S1G). By contrast, exposure to an LS + BS^{low} infection afforded full protection against lung pathology ($p < 0.0001$ vs. LS + BS^{high}) (Figures S1B–S1G). Collectively, our data show that exposure to an LS infection impacts the outcome of malaria, suggesting that the establishment of

Figure 1. *Plasmodium* cross-stage interplay determines the outcome of malaria

(A) Schematic representation of the protocol for LS + BS infections and assessed outcomes.

(B–H) Survival (left) and parasitemia (right) of WT C57BL/6 mice subjected to infections consisting of (B) salivary gland material of non-infected mosquitoes followed, 2 days later, by 10^6 (n = 20; 4 ind. exp.) or 10^4 (n = 10; 2 ind. exp.) PbANKA iRBCs, (C) 20,000 γ-irradiated PbANKA spz followed, 2 days later, by 10^6 (n = 19; 4 ind. exp.) or 10^4 (n = 10; 2 ind. exp.) PbANKA iRBCs, (D) 20,000 PbANKA *lisp2*$^-$ spz followed, 2 days later, by 10^6 (n = 15; 3 ind. exp.) or 10^4 (n = 10; 2 ind. exp.) PbANKA iRBCs, (E) 20,000 PbANKA *uis4*$^-$ spz followed, 2 days after, by 10^6 (n = 9; 2 ind. exp.) or 10^4 (n = 10; 2 ind. exp.) PbANKA iRBCs, (F) 5,000 γ-irradiated PbANKA spz followed, 2 days after, by 10^6 (n = 9; 2 ind. exp.) or 10^4 (n = 10; 2 ind. exp.) PbANKA iRBCs, (G) 1,000 γ-irradiated PbANKA spz followed, 2 days after, by 10^6 (n = 5; 1 ind. exp.) or 10^4 (n = 10; 2 ind. exp.) PbANKA iRBCs, and (H) 20,000 heat-killed PbANKA spz followed, 2 days after, by 10^6 (n = 10; 2 ind. exp.) or 10^4 (n = 10; 2 ind. exp.) PbANKA iRBCs.

(I) Representative microphotographs of hematoxylin and eosin stained sagittal sections through hindbrain and quantification of brain volume of non-infected (NI) C57BL/6 mice (n = 4) or following BS^{low} (n = 4), BS^{high} (n = 5), LS + BS^{low} (n = 5), and LS + BS^{high} (n = 4) infections. Height of the pons in WT C57BL/6 mice succumbing to ECM (red double arrow) following BS^{low}, BS^{high}, or LS + BS^{high} infections contrasted with that of NI C57BL/6 mice (black double arrow, corresponding to the normal height of the pons) or those subjected to a BS + LS^{low} infection (red arrowhead). Severe swelling of the hindbrain was often accompanied by the dilation of the 4th ventricle (4thV,*) and focally extensive cerebral necrosis (#). p, pons; m, medulla; and cb, cerebellum. Original magnification 1× (scale bars, 2.5 mm).

(J) Representative microphotographs of modified von Kossa stained coronal sections through olfactory bulb and quantification of hemorrhage area in the same experimental groups as in (I). Multifocal cerebral hemorrhage (black arrowheads) is seen in all experimental groups succumbing to ECM (BS^{low}, BS^{high}, and LS + BS^{high}) in contrast to NI and LS + BS^{low}-infected C57BL/6 mice. Original magnification 1× (scale bars, 2.5 mm).

(K) Schematic representation of the protocol used for exposure to multiple, low inoculum spz administrations followed by live spz infection and assessed outcomes.

(L) Survival (left), patency (middle), and parasitemia (right) of WT C57BL/6 mice receiving 4 (n = 10; 2 ind. exp.), 2 (n = 10; 2 ind. exp.), and 1 (n = 10; 2 ind. exp.) doses of 100 γ-irradiated PbANKA spz, or left unexposed (n = 5; 1 exp.) followed by infection with 500 PbANKA spz.

(M) Survival (left), patency (middle), and parasitemia (right) of C57BL/6 mice receiving 4 doses of 100 γ-irradiated PbANKA spz as in (L) followed by infection with 500 PbANKA spz 7 (n = 10; 2 ind. exp.), 60 (n = 10; 2 ind. exp.), or 120 (n = 10; 2 ind. exp.) days after the last dose. Only mice with established BS infection were included in the survival and parasitemia graphs.

(B–H, L, and M) Survival (log-rank test) and parasitemia (linear mixed-effects regression) are represented as the mean survival rate and mean percentage of iRBCs ± SEM, respectively.

(I and J) Data (unpaired t test with Welch's correction) are represented as box plot (min. to max.). For complete statistical analysis, please refer to Data S3.

See also Figure S1.

pathology does not rely solely on the BS of infection but rather on the integration of signals from both stages of parasite development. Further, it implies that protection from death following spz exposure depends on the fine-tuning of parasite burdens in both the hepatic and the erythrocytic stages of infection, i.e., a sufficiently high threshold of LS parasites coupled with low enough parasite density in the subsequent BS of infection.

In malaria-endemic areas, it is estimated that each individual may be exposed to up to 300 infectious mosquito bites per year.[11] The fact that, in rodents, spz inoculated during an ongoing BS infection establish within hepatocytes but become growth arrested and fail to develop into RBC-infective merozoites[12] opens the possibility that exposure to non-productive *Plasmodium* liver infections may also occur in humans during continuous re-infections in natural transmission settings. This, together with the notion that natural protection against malaria associates with the host's ability to limit the load of erythrocytic parasites,[6,7] led us to hypothesize that the LS of infection influences the incidence of severe disease under natural transmission conditions. In order to determine if that was the case, we assessed ECM establishment under physiological infection conditions following exposure to multiple spz infections (in the range of those expected under natural transmission conditions[13,14]) by inoculating non-productive spz prior to a natural infection (Figure 1K). Our results show that 4 administrations of 100 radiation-attenuated spz, interspaced by one week, were sufficient to afford complete protection from ECM following a subsequent infection with fully infectious spz (Figure 1L). The observed protective effect was dependent on the exposure rate, as protection dwindled to 70% ± 14.1% and 30% ± 14.1% upon two or a single spz exposure, respectively ($p < 0.0011$; single vs. 4 spz exposures). None of the spz exposure regimens provided sterile immunity or delayed patency ($p = 0.0614$; no exposure vs. 4 spz exposures) (Figure 1L). Additionally, protection against ECM upon exposure to spz waned over time with a decrease in host survival when spz exposure and infection were separated by 120 days ($p = 0.0103$) (Figure 1M). This is consistent with the notion that, even after it develops, clinical immunity in humans can be lost in 3–5 years in the absence of re-exposure.[15,16] Together, these data show that continued exposure to low-inoculum spz infections is sufficient to afford protection from severe pathology following a natural infection, in a dose- and time-dependent manner.

The outcome of *Plasmodium* infection relies on the liver stage-dependent activation of γδ T cells

Next, we sought to unveil the mechanism responsible for the observed protection from ECM. Since host hepatocytes initiate and propagate a type I interferon (IFN)-dependent response upon spz infection[3,4] and type I IFNs modulate disease severity[17,18] we assessed the contribution of type I IFN to the LS + BS^{low}-driven protection from ECM. Type I IFN receptor subunit 1-deficient mice (*Ifnar1*$^{-/-}$) showed similar clinical outcomes to wild-type (WT) mice when given LS + BS^{high}, LS + BS^{low}, or liver-mocked, BS infections (Figures S1H and S1I), showing that type I IFN was not required for the observed protection.

Cerebral malaria in both mice and humans is associated with the presence of $CD8^+$ T lymphocytes in the CNS.[19–21] Exposure to spz during the LS of infection can result in early priming and activation of potentially pathogenic effector $CD8^+$ and $CD4^+$ T lymphocytes specific for spz-derived or cross-stage antigens, thus biasing the immune response during the subsequent BS of infection.[22–24] Therefore, we asked whether the establishment of *Plasmodium* spz affected adaptive immune responses leading to ECM. Time-dependent analysis of the frequency of $CD8^+$ T lymphocytes in the CNS revealed kinetics of accumulation consistent with that of the emergence of clinical signs of ECM in both BS^{high} ($p < 0.0001$ vs. uninfected; day 7 post infection [p.i.]) and BS^{low} ($p = 0.0005$ vs. uninfected; day 8 p.i.) infections (Figure S1J). By contrast, mice subjected to an LS + BS^{high} infection exhibited an earlier accumulation of $CD8^+$ T lymphocytes in the CNS at a time when infiltration of adaptive immune cells was not noticeable in BS^{high}-infected mice ($p < 0.0001$; day 4 p.i.), which persisted until mice succumbed to ECM (Figure S1J). This was also the case during an LS + BS^{low} infection, where $CD8^+$ T lymphocytes accumulated, and persisted, at levels comparable with those of LS + BS^{high}-infected mice ($p = 0.2256$; day 4 p.i.) (Figure S1J). $CD4^+$ T lymphocyte accumulation in the CNS followed similar kinetics (Figure S1K). Pre-infective transfer of traceable, *Plasmodium* cross-stage antigen-specific PbT-1 $CD8^+$ T lymphocytes,[25] which are sufficient to cause ECM when transferred into mice lacking endogenous $CD8^+$ T lymphocytes,[23] resulted in similar numbers of these cells present in the CNS of protected mice undergoing an LS + BS^{low} infection when compared with those present in mice succumbing to ECM following either an LS + BS^{high} ($p = 0.4698$) or a BS^{low} ($p = 0.1010$) infection (Figure S1L). Moreover, endogenous $CD8^+$ and PbT-1 T lymphocyte activation and effector function, as assessed by the production of IFN-γ and granzyme B, did not differ significantly between all groups, independent of the clinical outcome of infection (Figures S1M and S1N). In summary, these data show that, even if liver infection precipitated $CD8^+$ T cell-driven inflammation, protection from ECM upon spz exposure acts independently of the accumulation of effector $CD8^+$ T lymphocytes in the CNS.

We next pursued the hypothesis that γδ T cells, which respond during *Plasmodium* liver stage,[26,27] are at the basis of protection from severe pathology following exposure to spz. To test this hypothesis, we made use of *Tcrδ*$^{-/-}$ mice, which are deficient for this particular cellular subset. Although the absence of γδ T cells had no impact on the clinical outcome when infection was initiated by iRBCs only, independent of the inoculum (Figures 2A, 2B, and S2A), protection from ECM, as afforded by the LS + BS^{low} infection in WT mice, was lost in *Tcrδ*$^{-/-}$ mice ($p = 0.0294$ vs. WT mice) (Figures 2C and S2A). By contrast, *Tcrδ*$^{-/-}$ mice failed to develop ECM when subjected to an LS + BS^{high} infection, whereas most WT mice succumbed to the neurological syndrome ($p = 0.0014$) (Figures 2D and S2A). Similarly to WT mice (Figures S1J, S1K, and S1M), the accumulation and activation of $CD8^+$ and $CD4^+$ T lymphocytes in the CNS of protected *Tcrδ*$^{-/-}$ mice following an LS + BS^{high} infection did not differ from that of ECM-succumbing WT controls (Figures S2B–S2D). Moreover, the LS-dependent protection from ECM in *Tcrδ*$^{-/-}$ mice also acted independently of the suppression of the BS parasitemia (Figures 2C and 2D), suggesting that protection from ECM following exposure to spz reflected a mechanism of host tolerance, rather than resistance, to infection.[28] Collectively, these data show that the integration

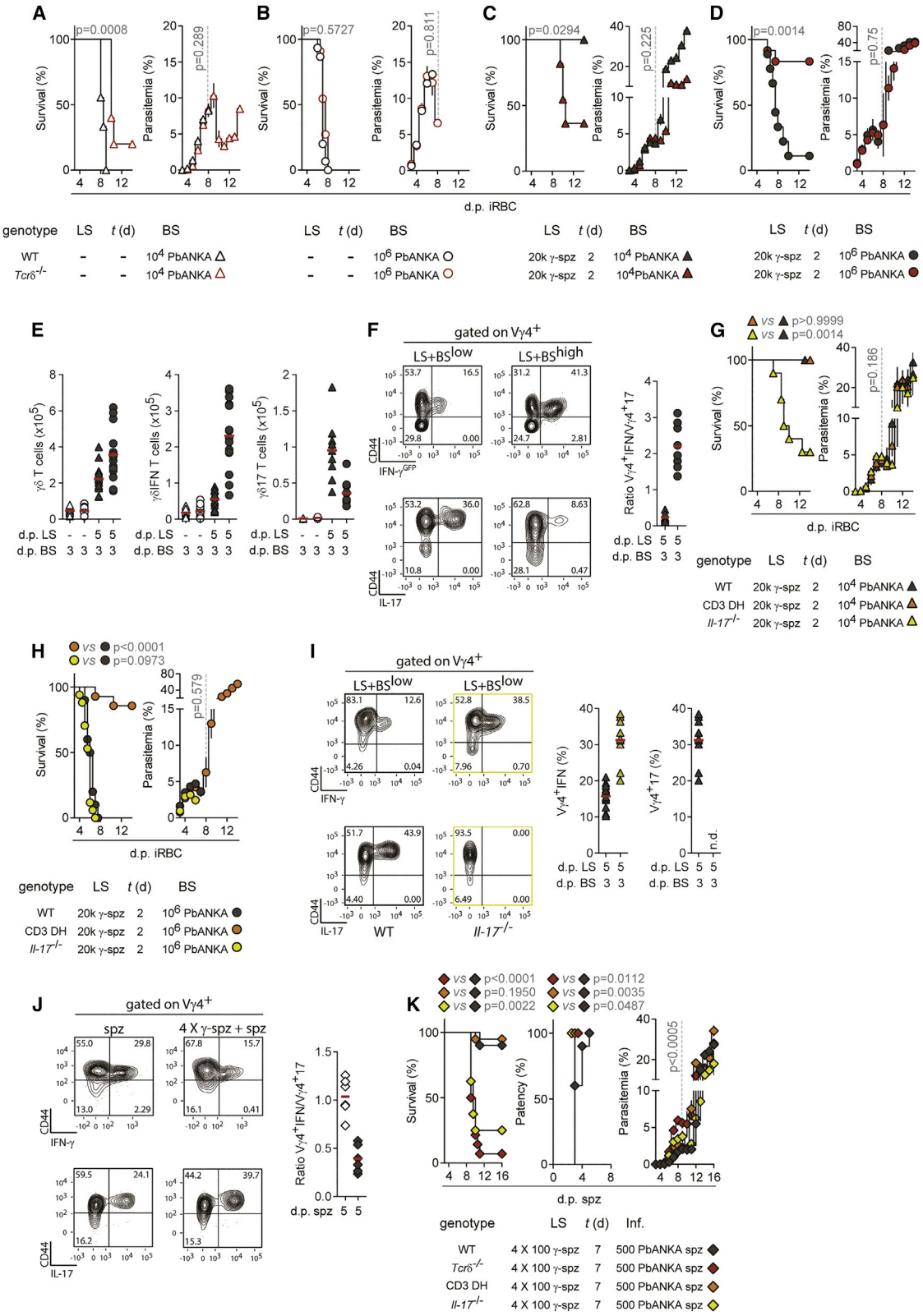

Figure 2. The outcome of *Plasmodium* infection relies on liver stage-dependent activation of distinct γδ T cell subsets

(A) Survival (left) and parasitemia (right) of WT (n = 9; 2 ind. exp.) and *Tcrδ*$^{-/-}$ (n = 5; 1 exp.) C57BL/6 mice subjected to BS^{low} infections.

(B) Survival (left) and parasitemia (right) of WT (n = 10; 2 ind. exp.) and *Tcrδ*$^{-/-}$ (n = 11; 3 ind. exp.) C57BL/6 mice subjected to BS^{high} infections.

(legend continued on next page)

of signals from both the liver and blood stages of infection, critical for the clinical outcome of infection, operates in a γδ T cell-dependent manner. In accordance, hepatic γδ T cells accumulated following LS + BS infections, when compared with BS infections alone, independent of the iRBC inoculum ($p < 0.0001$) (Figure 2E).

Functional specification of γδ T cells dictates protection or death

γδ T cells exhibit pleiotropic functional capacities, with the production of IFN-γ (γδIFN) and IL-17 (γδ17) defining the two predominant effector subsets.[29,30] Analysis of hepatic γδ T cell functional subsets revealed that γδIFN cells expanded in the liver of mice subjected to an LS + BS^{high} infection ($p < 0.0001$, LS + BS^{low} vs. LS + BS^{high}), whereas γδ17 cells predominated following an LS + BS^{low} infection ($p = 0.0004$, LS + BS^{low} vs. LS + BS^{high}) (Figure 2E). This functional dichotomy was particularly evident in activated ($CD44^+$) $V\gamma4^+$ γδ T cells, which exhibited decreased levels of IFN-γ and increased production of IL-17 when isolated from the livers of mice subjected to an LS + BS^{low} infection (Figure 2F). Conversely, liver $V\gamma4^+$ γδ T cells from mice subjected to LS + BS^{high} infection produced mostly IFN-γ, inverting the ratio between γδIFN and γδ17 cells (Figure 2F). In contrast to $V\gamma4^+$ γδ T cells, the ratio between IFN-γ and IL-17 producers among $V\gamma1^+$ γδ T cells was not altered between mice that succumbed, or not, to ECM (Figure S2E). The production of IL-17 in the liver was restricted to $V\gamma4^+$ γδ T cells, with a negligible contribution of liver-infiltrating $CD4^+$ T lymphocytes (Figure S2F). Collectively, these results show that altered ratios of γδ17 and γδIFN T cells associate with protection from, or establishment of, ECM.

Given the association between the differential accumulations of γδIFN vs. γδ17 cells within the $V\gamma4^+$ γδ T cell compartment and the opposing outcomes of infection, we hypothesized that this functional dichotomy explains the phenotypic dichotomy afforded by the crosstalk between the LS and BS of infection on the establishment of severe pathology (LS + BS^{low} vs. LS + BS^{high}, Figures 1C–1E). Consistent with this, *Il-17*$^{-/-}$ mice behaved similarly to *Tcrδ*$^{-/-}$ mice (Figure 2C), succumbing to ECM when subjected to an LS + BS^{low} infection ($p = 0.0014$ vs. WT mice) (Figures 2G and S2A). This was, however, not the case for CD3γ and CD3δ double-haploinsufficient (CD3DH; *Cd3γ*$^{+/-}$ *Cd3δ*$^{+/-}$) mice, shown to have reduced peripheral γδIFN T cells,[31] which were as protected from ECM after an LS + BS^{low} infection as WT mice (Figures 2G and S2A). Conversely, all *Il-17*$^{-/-}$ mice succumbed to ECM when subjected to an LS + BS^{high} infection, similarly to WT mice, whereas CD3DH mice behaved akin to *Tcrδ*$^{-/-}$ mice (Figure 2D) and mostly failed to develop ECM upon LS + BS^{high} infection ($p < 0.0001$ vs. WT mice) (Figures 2H and S2A). As in *Tcrδ*$^{-/-}$ mice (Figures 2C, 2D, and S2B–S2D), the opposing outcomes of infection were not associated with differences in parasitemia ($p = 0.186$ and $p = 0.579$ in LS + BS^{low} and LS + BS^{high} infections, respectively) (Figures 2G and 2H) or with the pattern of $CD8^+$ and $CD4^+$ T lymphocyte accumulation and activation in the CNS (Figures S2B–S2D). None of these cellular/molecular factors were found to be relevant for the establishment of ECM following a liver-mocked, BS infection, irrespective of the initial iRBC inoculum (Figures S2A, S2G, and S2H). Absence of IL-17 associated with increased frequency of IFN-γ producers within liver $V\gamma4^+$ (Figure 2I), but not $V\gamma1^+$ (Figure S2I), γδ T cells following an LS + BS^{low} infection. This suggests that pathogenic IFN-γ production by γδ T cells is the default functional specification pathway during the BS of infection, which is countered by γδ17 T cells. In conclusion, the observed dichotomy of the outcome of infection relied on the LS-dependent activation of $V\gamma4^+$ γδ T cells, which exhibited distinct cytokine profiles selectively sustained by different blood stage parasite loads, i.e., host survival relied on γδ T cells and IL-17 production, and thus γδ17 T cells, whereas γδIFN T cells were responsible for ECM establishment. Our findings employing the LS + BS infection model were corroborated following exposure to multiple, low-inoculum infections with non-productive spz prior to a natural infection (Figures 1L and 1M), which resulted in a similar pattern of cytokine production (Figures 2J and S2J), with γδ T cells and IL-17 production being critical for protection from ECM (Figure 2K).

(C) Survival (left) and parasitemia (right) of WT (n = 10; 2 ind. exp.) and *Tcrδ*$^{-/-}$ (n = 11; 2 ind. exp.) C57BL/6 mice subjected to LS + BS^{low} infections.
(D) Survival (left) and parasitemia (right) of WT (n = 9; 2 ind. exp.) and *Tcrδ*$^{-/-}$ (n = 12; 3 ind. exp.) C57BL/6 mice subjected to LS + BS^{high} infections.
(E) Quantification of γδ (left), γδIFN (middle), and γδ17 (right) T cells isolated from the liver of WT C57BL/6 mice subjected to BS^{low} (open triangles), BS^{high} (open circles), LS + BS^{low} (black triangles), and LS + BS^{high} (black circles) infections, 3 days after transfusion of iRBCs. Cell gating strategy shown in Figure S5C.
(F) Representative flow cytometry plots of the production of IFN-γ (upper row) and IL-17 (bottom row) and the ratio between γδIFN and γδ17 cells in $V\gamma4^+$ γδ T cells isolated from the liver of WT C57BL/6 mice subjected to LS + BS^{low} (black triangles) or LS + BS^{high} (black circles) infections, 3 days after transfusion of iRBCs. Cell gating strategy shown in Figure S5C.
(G) Survival (left) and parasitemia (right) of WT (n = 9; 2 ind. exp.), CD3DH (n = 8; 2 ind. exp.), and *Il-17*$^{-/-}$ (n = 14; 2 ind. exp.) C57BL/6 mice subjected to LS + BS^{low} infections.
(H) Survival (left) and parasitemia (right) of WT (n = 10; 2 ind. exp.), CD3DH (n = 14; 3 ind. exp.), and *Il-17*$^{-/-}$ (n = 18; 3 ind. exp.) C57BL/6 mice subjected to LS + BS^{high} infections.
(I) Representative flow cytometry plots and relative abundance of γδIFN and γδ17 cells in $V\gamma4^+$ γδ T cells isolated from livers of WT (black triangles) and *Il-17*$^{-/-}$ (yellow triangles) C57BL/6 mice subjected to an LS + BS^{low} infection, 3 days after transfusion of iRBCs. Cell gating strategy shown in Figure S5C.
(J) Representative flow cytometry plots and the ratio between γδIFN and γδ17 cells in $V\gamma4^+$ γδ T cells isolated from the liver of WT C57BL/6 mice receiving 4 doses of salivary gland material of non-infected mosquitoes (open diamonds) or 4 doses of 100 γ-irradiated PbANKA spz (black diamonds) followed by infection with 500 PbANKA spz, 5 days after live spz infection. Cell gating strategy shown in Figure S5C.
(K) Survival (left), patency (middle), and parasitemia (right) of WT (n = 10; 2 ind. exp.), *Tcrδ*$^{-/-}$ (n = 14; 3 ind. exp.), CD3DH (n = 19; 3 ind. exp.), and *Il-17*$^{-/-}$ (n = 8; 2 ind. exp.) C57BL/6 mice receiving 4 weekly doses of 100 γ-irradiated PbANKA spz followed, 7 days after, by infection with 500 PbANKA spz.
(A–D, G, H, and K) Survival (log-rank test) and parasitemia (linear mixed-effects regression) are represented as the mean survival rate and mean percentage of iRBCs ± SEM, respectively.
(E, F, I, and J) Data are represented as dot-plot; red line represents mean. For complete statistical analysis, please refer to Data S3.
See also Figures S2 and S5.

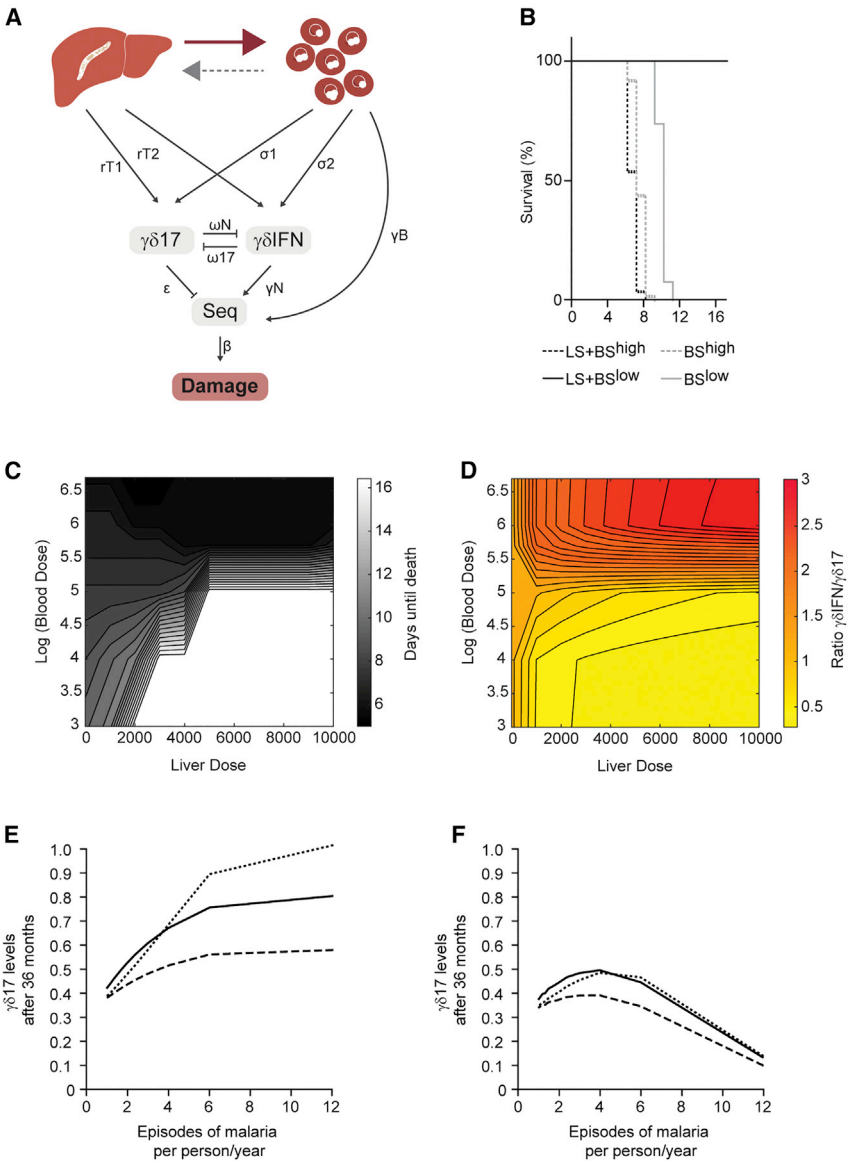

Figure 3. Mathematical model recapitulating the interactions between parasite developmental stages on host mortality and theoretical predictions

(A) Schematic representation of the within-host model. In this model, BS parasites replicate and contribute to the development of pathology. LS sporozoites stimulate the activation and proliferation of IL-17- or IFN-γ-producing γδ T cells in a manner dependent on feedback from BS density. The density of each γδ T cell subtype promotes its own continued proliferation but γδ17 cells inhibit the proliferation of their γδIFN counterparts. γδ17 cells promote processes that decrease the progression to ECM ("damage").

(B) Simulated survival of hosts subjected to BS^{high} or BS^{low} infections alone or following an inoculum of LS infection.

(C) The predicted interaction of LS by BS on mortality rates (days until death) on a continuous scale (dark, die; white, survive).

(D) The predicted ratio of γδIFN and γδ17 cells over LS by BS parameter space. Red indicates the predominance of γδIFN cells, whereas yellow indicates the predominance of γδ17 cells. At high BS density, γδ T cells are quickly coerced toward high IFN-γ-producing ratios, while at low BS density, IL-17 producers have time to inhibit the proliferation of IFN-γ-producing cells before BS levels reach a sufficient density to engage them.

(E and F) The predicted impact of transmission frequency (malaria infections per year) on the production of protective γδ17 cells in competition with γδIFN cells. (E) In a low exhaustion index scenario ($\kappa_i = 0.04$), frequent episodes of infection result in an increased, near-maximal level of γδ17 cells, particularly when the ability of γδIFN cells to inhibit γδ17 is asymmetrically low (dotted line) compared with situations where both subtypes minimally inhibit each other (solid line) or strongly inhibit each other (dashed line). (F) Under high rates of γδ T cell subtype exhaustion, protective γδ17 cell frequency is maximized at intermediate exposure frequencies regardless of symmetry and strength of T cell subtype inhibition.

See also Tables S1 and S2 and Data S1 and S2.

To further clarify our conceptual understanding of the potential feedbacks governing the crosstalk between both stages of parasite development and the distinct γδ T cell subsets, we created a mathematical model of coupled ordinary differential equations representing the hypothetical players in the system (Figure 3A; Data S1). Our within-host model closely recapitulated the empirical observations of interactions between parasite developmental stages on host mortality (Figure 3B). This prediction held over a continuous distribution of LS by BS interaction effects and reflected the ratio of γδ17 to γδIFN cells (Figures 3C and 3D). Such dependency relied on the assumption that γδIFN cells have a faster BS-dependent proliferation rate (Table S1), consistent with their enhanced responses to T cell receptor stimulation in mice[32] and the notion that they are more sensitive to *Plasmodium*-derived phosphoantigen recognition in humans.[33,34]

Previous studies in humans note an association between asymptomatic malaria episodes and reduced levels of circulating IFN-γ-producing Vγ9Vδ2 T cells, which are suggested to become exhausted in frequently exposed individuals.[35–37] However, our experimental data (Figures 2F–2K), supported by our within-host model (Figures 3B–3D) raised the possibility that γδ17 T cells may negatively regulate the expansion of damage-promoting IFN-γ producers while also promoting tolerance. To address this question, we built a discrete-time model of γδ T cell interactions to predict γδ17 dynamics over a 3-year period for hosts that vary in the average frequency of malaria infection, from one episode per month to one per year (Data S2). We varied the probability of γδ T cell exhaustion per infection event and the relative intensity of reciprocal negative regulation among γδIFN and γδ17 T cells (Figures 3E and 3F). Our simulations suggest that in the absence of exhaustion (Figure 3E), γδ17 T cell

frequency increased with exposure frequency, particularly when inhibition by γδIFN is relatively inefficient. The accumulation of exhaustion markers by γδ T cells with repeated exposure resulted in the highest levels of γδ17 at intermediate transmission frequencies and may be sufficient to explain the observed decline in γδIFN T cell levels with increasing infection frequency in human populations. This role of γδ17 cells is potentially reflected in the fact that protection from severe manifestations of malaria and death is established fast and after only a few exposures to *Plasmodium* infection.[16]

γδ T cells and IL-17 promote splenic erythropoiesis and reticulocytosis

Next, we sought to understand how γδ17 cells mediate protection from severe CNS pathology. During our investigations, we unexpectedly observed that WT mice subjected to an LS + BS^{low} infection exhibited an increase in spleen size, when compared with both *Tcrδ*$^{-/-}$and *Il-17*$^{-/-}$ mice ($p = 0.0002$ and $p < 0.0001$, respectively) (Figure 4A). Further, γδ T cell accumulation, assessed by functional luciferase expression in *Tcr*δ-GDL mice,[38] was evident as early as 2 days p.i. in the spleen of WT mice subjected to an LS + BS^{low}, but not an LS + BS^{high}, infection ($p = 0.0012$ and $p = 0.5134$ vs. NI mice, respectively) (Figure 4B), evidencing that γδ T cell accumulation in the spleen was associated with protection from severe pathology. A critical role for the spleen in ECM protection upon exposure to spz infection was demonstrated by the complete loss of protection in splenectomized (SPX) mice subjected to an LS + BS^{low} infection ($p < 0.0001$ vs. sham-operated mice) (Figure 4C), which exhibited the pathological hallmarks of ECM (Figures S3A and S3B). Likewise, surgical removal of the spleen prior to exposure to multiple, low-inoculum infections with non-productive spz followed by an infection with fully infectious spz resulted in a complete loss of protection from ECM (Figure 4D). A thorough analysis of the different cellular subsets in the spleen following an LS + BS^{low} infection revealed that, contrary to both *Tcrδ*$^{-/-}$ and *Il-17*$^{-/-}$ mice, WT mice exhibited an increase, both in absolute numbers ($p = 0.0005$ and $p < 0.0001$ vs. WT mice, respectively) and relative frequency ($p = 0.0004$ and $p < 0.0001$ vs. WT mice, respectively), of erythrocyte progenitors (erythroblasts) on the days preceding the onset of ECM (Figures 4E–4G). Consequently, we observed an increased frequency of circulating young (CD71^{+}) reticulocytes in ECM-protected WT mice, contrasting with *Tcrδ*$^{-/-}$ and *Il-17*$^{-/-}$ mice, where the frequency of CD71^{+} reticulocytes decreased steadily throughout LS + BS^{low} infection until mice succumbed to ECM (Figure 4H). Further corroborating that the observed production of reticulocytes following exposure to spz was sustained by the spleen is (1) the lack of CD71^{+} reticulocyte emergence in the peripheral blood of WT SPX, but not of sham-operated, mice subjected to an LS + BS^{low} infection (Figure S3C) or exposed to low-inoculum infections with non-productive spz prior to a natural infection (Figure S3D) and (2) the severe reduction of erythroblasts in the bone marrow of WT, *Tcrδ*$^{-/-}$ and *Il-17*$^{-/-}$ mice, irrespective of the outcome of infection (Figures S3E–S3G). At later stages of infection, splenic erythroblasts further expanded in protected WT mice pre-exposed to spz, while bone marrow erythropoiesis remained impaired (Figures S3H–S3J). This was also the case in the small cohort of *Tcrδ*$^{-/-}$ and *Il-17*$^{-/-}$ mice surviving an LS + BS^{low} infection (Figures S3H–S3J). Taken together, our data show that protection from ECM following an LS + BS^{low} infection is associated with splenic erythropoiesis and concomitant reticulocytosis in a γδ T cell- and IL-17-dependent manner.

Increased reticulocyte availability curtails the development of ECM

To test whether the observed increased reticulocytosis was at the basis of protection, we resorted to the antibody-mediated engagement of the stress sensor CD24, which results in erythroid progenitor expansion in the spleen[39] and in the subsequent transient elevation of reticulocyte numbers in the circulation of WT, *Tcrδ*$^{-/-}$, and *Il-17*$^{-/-}$ mice (Figure S4A). Administration of αCD24 mouse antibody prevented severe neuropathology following a natural infection of WT mice ($p < 0.0001$ vs. IgG2b administration) (Figures 5A and S4B) and restored protection from ECM in *Tcrδ*$^{-/-}$ and *Il-17*$^{-/-}$ mice subjected to an LS + BS^{low} infection ($p < 0.0001$ and $p = 0.0001$ vs. IgG2b administration in *Tcrδ*$^{-/-}$ and *Il-17*$^{-/-}$ mice, respectively) (Figures 5B, 5C, S4C, and S4D). Increased reticulocytosis following αCD24 treatment prevented ECM in the absence of an LS infection, as shown by the protection conferred to hosts receiving solely a BS^{low} infection, irrespective of their genotype (Figures 5D–5F and S4E–S4G). Therapeutic increase of circulating reticulocytes by the adoptive transfer of full blood obtained from donors treated with phenylhydrazine into WT mice infected with fully infectious spz, starting 5 days p.i., was sufficient to curb ECM establishment while the transfer of equivalent amounts of RBCs failed to do so (Figures 5G and S4H). This was also the case upon adoptive transfer of reticulocyte-enriched blood, but not of RBCs, into *Tcrδ*$^{-/-}$ and *Il-17*$^{-/-}$ mice receiving an LS + BS^{low} infection (Figures 5H, 5I, S4I, and S4J). Analysis of circulating reticulocytes following adoptive transfer revealed that a substantial proportion of transferred CD71^{+} reticulocytes was readily infected 4 h post transfer and became almost undetectable on the following day prior to a new adoptive transfer (Figures S4H–S4J). The rapid exhaustion of circulating reticulocytes upon adoptive transfer may reflect the preference of PbANKA to invade reticulocytes over normocytes and the fast remodeling of reticulocytes upon invasion, with concomitant loss of CD71 expression.[40,41]

Adherence of *Plasmodium* iRBCs to the vascular endothelium, referred to as sequestration, is a crucial event for the onset of malaria pathology.[42,43] Thus, we next asked whether parasite sequestration was affected by reticulocyte availability. Our results show that following an LS + BS^{low} infection, *Il-17*$^{-/-}$ mice receiving RBCs from days 5 to 7 p.i. exhibited increased sequestration of iRBCs in the CNS ($p = 0.0016$ vs. WT mice), whereas the adoptive transfer of reticulocytes lowered this to levels comparable with those of LS + BS^{low}-infected WT mice ($p = 0.0517$) (Figure 5J) with consequent protection from ECM (Figure 5I).

DISCUSSION

We showed that *Plasmodium* cross-stage interplay dictated malaria outcome via γδ T cells and that IL-17-promoted stress erythropoiesis was at the basis of disease protection. Our data reinforce the notion that the pathophysiology of severe malaria following *Plasmodium* infections initiated by spz is distinct from that ensuing after the transfusion of iRBCs, as recently shown in a controlled human malaria infection (CHMI) model,[44] and is in line with observations where altered parasite and host factors

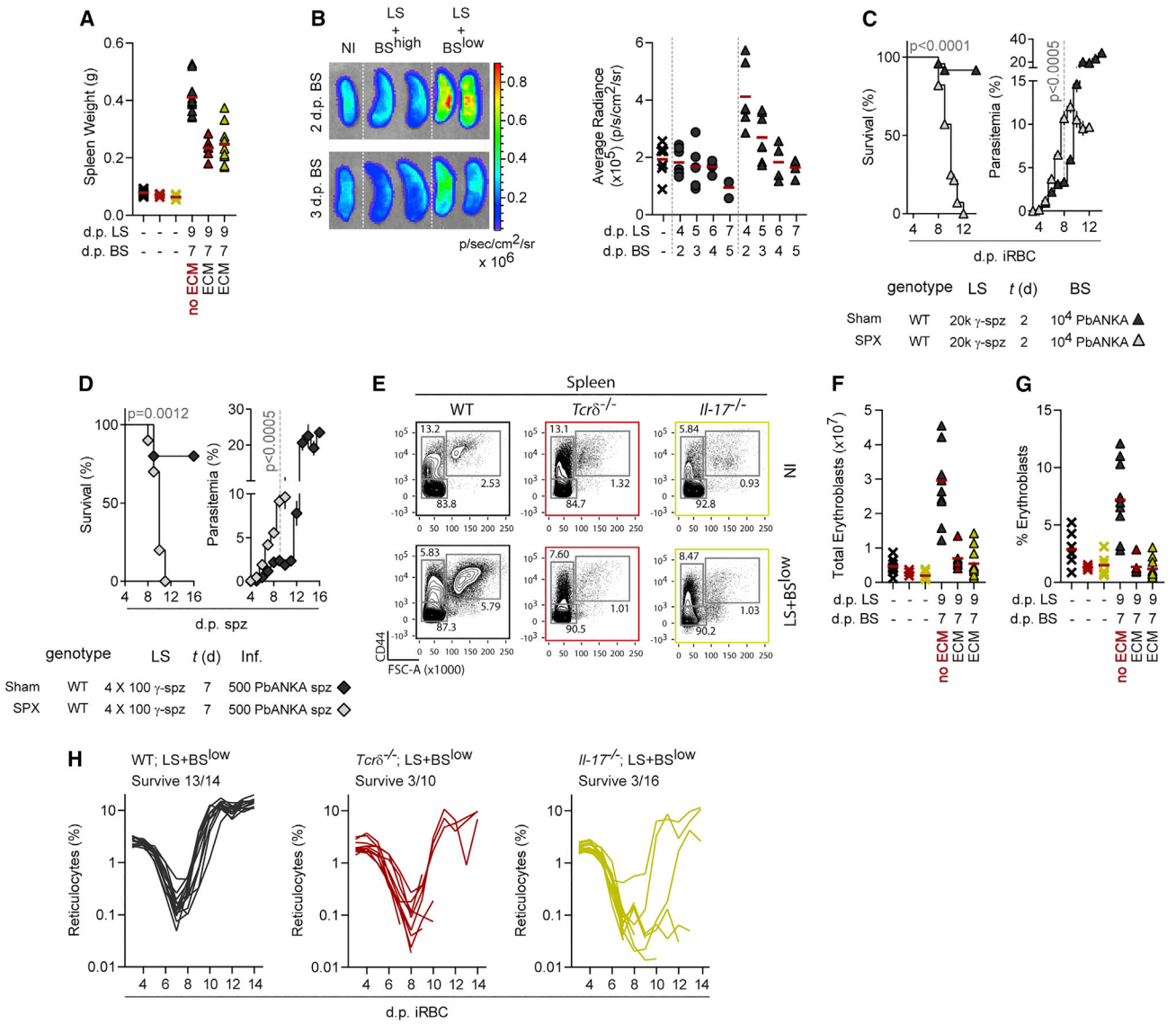

Figure 4. γδ T cells and IL-17 promote splenic erythropoiesis and reticulocytosis during *Plasmodium* infections

(A) Quantification of spleen weight of WT (black), *Tcrδ*$^{-/-}$ (red), and *Il-17*$^{-/-}$ (yellow) C57BL/6 mice, either non-infected (cross) or subjected to LS + BS^{low} (triangles) infection, 7 days after transfusion of iRBCs.

(B) Representative spleen bioluminescence images (left) and time-dependent quantification of functional luciferase expression (right) in γδ T cells in non-infected *Tcrδ*-GDL C57BL/6 mice (cross), or following LS + BS^{high} (black circles) or LS + BS^{low} (black triangles) infections.

(C) Survival (left) and parasitemia (right) of sham-operated (Sham) (n = 24; 4 ind. exp.) or splenectomized (SPX) (n = 29; 5 ind. exp.) C57BL/6 mice subjected to LS + BS^{low} infections.

(D) Survival (left) and parasitemia (right) of sham-operated (Sham) (n = 10; 2 ind. exp.) or splenectomized (SPX) (n = 10; 2 ind. exp.) C57BL/6 mice receiving 4 weekly doses of 100 γ-irradiated PbANKA spz followed by infection with 500 PbANKA spz.

(E) Representative flow cytometry plots of erythroblast accumulation in the spleen of WT (left column), *Tcrδ*$^{-/-}$ (middle column), and *Il-17*$^{-/-}$ (right column) C57BL/6 mice, either non-infected (NI) (upper row) or subjected to LS + BS^{low} infection (bottom row), 7 days after transfusion of iRBCs. Cell gating strategy shown in Figure S5D.

(F and G) (F) Quantification and (G) relative abundance of erythroblasts in the spleen of WT (black), *Tcrδ*$^{-/-}$ (red), and *Il-17*$^{-/-}$ (yellow) C57BL/6 mice, either non-infected (cross) or subjected to LS + BS^{low} infection (triangles), 7 days after transfusion of iRBCs. Cell gating strategy shown in Figure S5D.

(H) Time-dependent quantification of the relative abundance of reticulocytes in the peripheral blood of WT (left; black) (n = 14; 3 ind. exp.), *Tcrδ*$^{-/-}$ (middle; red) (n = 10; 2 ind. exp.), and *Il-17*$^{-/-}$ (right; yellow) (n = 16; 3 ind. exp.) C57BL/6 mice subjected to LS + BS^{low} infection. Cell gating strategy shown in Figure S5E.

(A, B, F, and G) Data are represented as dot-plot; red line represents mean.

(C and D) Survival (log-rank test) and parasitemia (linear mixed-effects regression) are represented as the mean survival rate and mean percentage of iRBCs ± SEM, respectively.

(H) Lines represent individual mice. For complete statistical analysis, please refer to Data S3.

See also Figures S3 and S5.

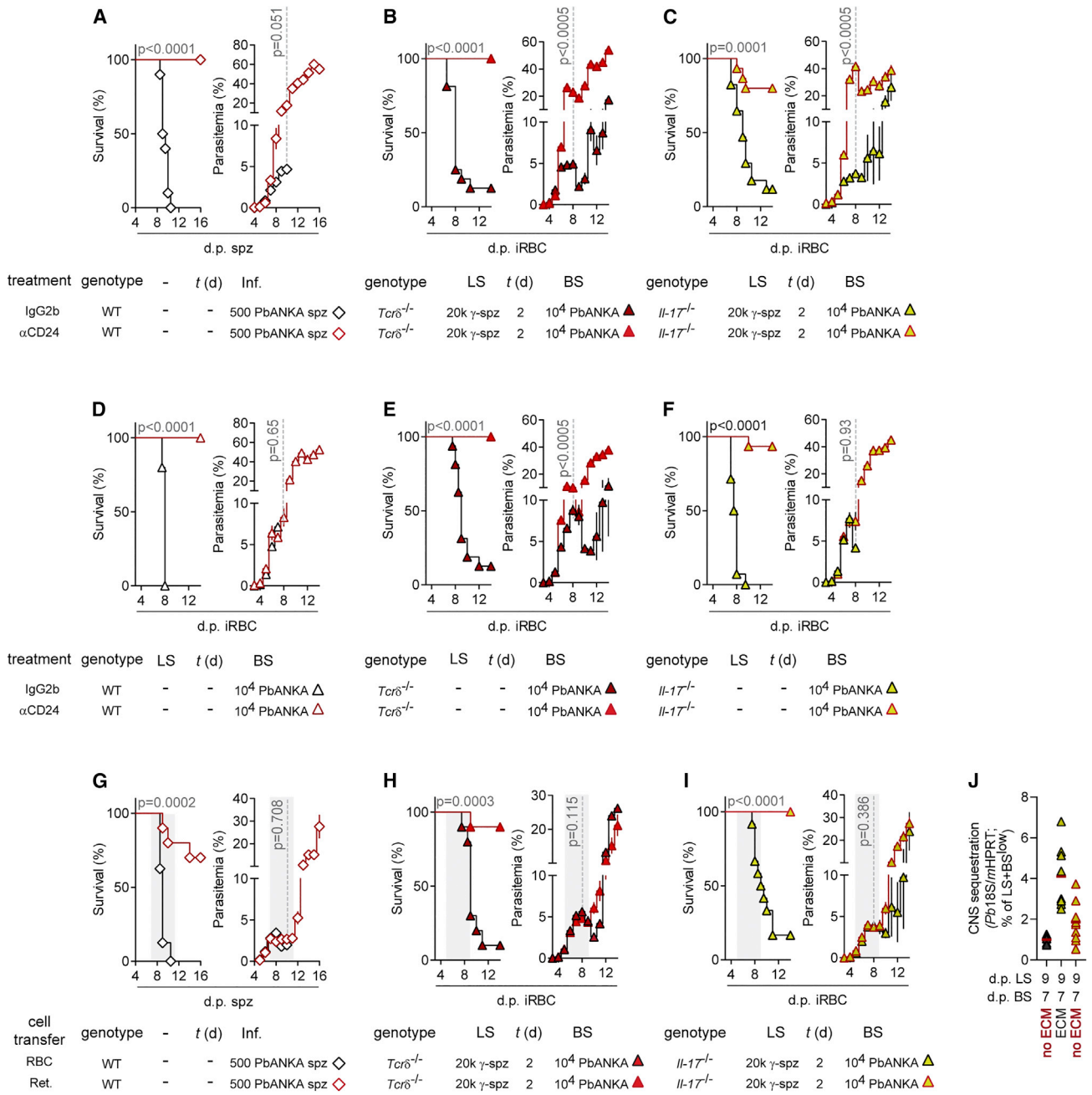

Figure 5. Increased reticulocyte availability curtails the development of ECM

(A) Survival (left) and parasitemia (right) of WT C57BL/6 mice receiving αCD24 (n = 9; 2 ind. exp.) or isotype control (n = 10; 2 ind. exp.) antibodies 4 h after infection with 500 PbANKA spz.

(B and C) Survival (left) and parasitemia (right) of (B) *Tcrδ*$^{-/-}$ or (C) *Il-17*$^{-/-}$ C57BL/6 mice subjected to LS + BS^{low} infection and receiving αCD24 (*Tcrδ*$^{-/-}$ n = 16; 3 ind. exp., *Il-17*$^{-/-}$ n = 15; 3 ind. exp.) or isotype control (*Tcrδ*$^{-/-}$ n = 16; 3 ind. exp., *Il-17*$^{-/-}$ n = 17; 3 ind. exp.) antibodies on the day of spz exposure.

(D–F) Survival (left) and parasitemia (right) of (D) WT, (E) *Tcrδ*$^{-/-}$, or (F) *Il-17*$^{-/-}$ C57BL/6 mice subjected to BS^{low} infection and receiving αCD24 (WT n = 14; 3 ind. exp., *Tcrδ*$^{-/-}$ n = 12; 2 ind. exp., *Il-17*$^{-/-}$ n = 15; 3 ind. exp.) or isotype control (WT n = 10; 3 ind. exp.; *Tcrδ*$^{-/-}$ n = 15; 3 ind. exp., *Il-17*$^{-/-}$ n = 14; 3 ind. exp.) antibodies 2 days before transfusion of iRBCs.

(G) Survival (left) and parasitemia (right) of C57BL/6 mice following infection with 500 PbANKA spz, and receiving daily adoptive transfers of 2 × 10^8 reticulocytes (Ret) (n = 10; 2 ind. exp.) or equivalent amounts of RBC (n = 8; 2 ind. exp.) from days 7 to 11 after infection (represented by gray area).

(H and I) Survival (left) and parasitemia (right) of (H) *Tcrδ*$^{-/-}$ and (I) *Il-17*$^{-/-}$ C57BL/6 mice subjected to LS + BS^{low} infection, receiving daily adoptive transfers of 2 × 10^8 reticulocytes (Ret) (*Tcrδ*$^{-/-}$ n = 10; 2 ind. exp., *Il-17*$^{-/-}$ n = 15; 3 ind. exp.) or equivalent amounts of RBC (*Tcrδ*$^{-/-}$ n = 10; 2 ind. exp., *Il-17*$^{-/-}$ n = 12; 3 ind. exp.) from days 5 to 9 after transfusion of iRBCs (represented by gray area).

(legend continued on next page)

set apart the course and outcome of infections initiated by the two distinct routes.[26,45] Although the integration of signals from both the liver and blood stages of infection dictated the clinical outcome of infection, the mechanism of protection seemed to occur entirely during the erythrocytic stage of parasite development. The production of IL-17 by γδ T cells induced extra-medullary erythropoiesis and concomitant reticulocytosis throughout the BS of infection, which was capable of protecting mice from ECM. Of note, increased levels of erythropoietin, which is essential for the differentiation of erythroid cells, are correlated with protection from severe disease in both humans[46] and rodents.[47,48] Although others attribute the protective role of erythropoietin in ECM to its neuroprotective and immune-modulatory functions,[47–49] our findings support the possibility that increasing erythropoietin levels may contribute to host survival during *Plasmodium* infections[50] by stimulating erythropoiesis and the *de novo* production of reticulocytes. Here, we showed that the increased availability of reticulocytes during infection reduced the accumulation of parasitized RBC in target organs. Given the central role of iRBC sequestration in the establishment of severe malarial pathology,[20] we postulate that such reduction mediates the observed protection from ECM. Such protection was decoupled from the activation and accumulation of effector $CD8^+$ T cells in the CNS.

Upon their first encounter with malaria parasites, individuals almost invariably develop a febrile illness which, if left untreated, may evolve into severe, and sometimes fatal, complications. For populations living in malaria-endemic areas, the risk of severe disease and death is highest in young children and declines rapidly.[6] Susceptibility to non-life-threatening clinical episodes of malaria continues but falls steadily such that by early adulthood febrile episodes are few and mild. Still, the risk of infection continues throughout life, implying that the acquisition of immunity to disease is distinct from that of immunity to the parasite. Although immune responses could potentially target any stage of the parasite to which humans are exposed to, most research focuses on the concept that naturally acquired immunity is predominantly against BSs, with no involvement of pre-erythrocytic stages. Our data have challenged this concept. Using rodent models of infection, supported by mathematical modeling, our findings imply that the ratio between γδIFN and γδ17 cells, triggered by exposure to hepatotropic parasites and specified by distinct circulating parasite burdens, is a critical determinant of the onset of severe disease among frequently exposed individuals living in moderate-to-high malaria transmission regions. Accordingly, multiple human population studies report a negative relationship between the frequency of malaria episodes per year and the levels of IFN-γ-producing Vγ9Vδ2 T cells,[35–37] with children with the lowest levels of this particular γδ T cell subset more likely to have asymptomatic malaria episodes, while those with the highest levels being symptomatic.[35] Moreover, genetic studies on IL-17F and IL-17RA polymorphisms in African populations suggest a protective role for this molecular pathway against CM,[51] further supporting our model. Thus, boosting IL-17 responses may constitute a promising strategy to tackle disease severity in endemic areas of *Plasmodium* infection.

Limitations of the study

Our study disclosed that the clinical outcome of *Plasmodium* infections is dictated by the integration of signals from both stages of parasite development within the mammalian host. Protection from severe malarial neuropathology afforded by the pre-exposure to hepatotropic forms of the parasite prior to low iRBC inoculum is mediated by γδ T cells and IL-17. A limitation of the study relies on the associative nature of these findings due to the current lack of appropriate genetic models allowing for the specific deletion of IL-17-producing γδ T cells.[52,53] Of note, γδ T cells were the major source of IL-17 in the liver following ECM-protective, LS + BS^{low} infections, with negligible contributions of other IL-17-producing cell types, including of $CD4^+$ T cells. Although protection is lost in the majority of $Tcr\delta^{-/-}$ and $Il\text{-}17^{-/-}$ mice, a small proportion still survive. This suggests that additional factor(s) play a residual role in protection from ECM following pre-exposure to spz, which was not addressed in our study.

Based on our experimental data obtained using rodent models of infection, and our mathematical simulations, we propose that IL-17-producing γδ T cells, i.e., γδ17 cells, are at the basis of protection from severe malaria manifestations in frequently exposed humans living in endemic areas. Subsequent studies in human populations are needed to evaluate whether this is, in fact, the case.

STAR★METHODS

Detailed methods are provided in the online version of this paper and include the following:

- KEY RESOURCES TABLE
- RESOURCE AVAILABILITY
  - Lead contact
  - Materials availability
  - Data and code availability
- EXPERIMENTAL MODEL AND SUBJECT DETAILS
  - Mice
  - Parasites
- METHOD DETAILS
  - Infections
  - ECM assessment
  - Histopathology and Stereology
  - PbT-1 $CD8^+$ T cell isolation and adoptive transfer
  - Isolation of tissue-infiltrating leukocytes
  - Flow cytometry
  - In vivo αCD24 antibody administration

(J) Parasite accumulation/sequestration in the CNS following an LS + BS^{low} infection, assessed by detection of PbANKA *18 s* ribosomal RNA by qRT-PCR of WT (black triangles) and $Il\text{-}17^{-/-}$ C57BL/6 mice receiving adoptive transfer of 2×10^8 reticulocytes (Ret) (yellow triangles, red line) or equivalent amounts of RBC (yellow triangles, black line, except WT) on days 5, 6, and 7 after infection. Mice were culled 4 h after adoptive cell transfer, 7 days after transfusion of iRBCs. (A–I) Survival (log-rank test) and parasitemia (linear mixed-effects regression) are represented as the mean survival rate and mean percentage of iRBCs ± SEM, respectively.

(J) Data are represented as dot-plot; red line represents mean. For complete statistical analysis, please refer to Data S3.

See also Figure S4.

- Adoptive transfer of cells
- Real time bioluminescence imaging
- Splenectomy
- RNA isolation and quantitative reverse-transcriptase PCR
- Within-host model
- Modelling the influence of transmission frequency on $\gamma\delta$ T cell dynamics

- QUANTIFICATION AND STATISTICAL ANALYSIS

SUPPLEMENTAL INFORMATION

Supplemental information can be found online at https://doi.org/10.1016/j.immuni.2023.01.031.

ACKNOWLEDGMENTS

We would like to acknowledge Freddy Frischknecht (Integrative Parasitology Center for Infectious Diseases, Heidelberg) for providing the *Plasmodium berghei lisp2*$^{-}$ parasite line, Immo Prinz (Hannover Medical School, Hannover) for providing genetically modified mouse lines, Ana Parreira (iMM-JLA, Portugal) and Geoff McFadden's lab (School of BioSciences, University of Melbourne, Australia) for mosquito rearing and infection with *Plasmodium* parasites, Helena Pinheiro (iMM-JLA, Portugal) for assistance with graphical design, Inês Bento and Miguel Prudêncio for critically reviewing this manuscript, and the Flow Cytometry and Rodent Facilities teams (iMM-JLA, Portugal) for their assistance. Work at iMM-JLA was supported by Fundação para a Ciência e a Tecnologia. Portugal (PTDC/MED-IMU/28664/2017) and the "La caixa" Banking Foundation, Spain (HR17-00264-PoEMM) grants attributed to Â.F.C. and M.M.M., respectively. Work at the Department of Microbiology and Immunology, The University of Melbourne, Australia, was funded by the National Health and Medical Research Council, Australia (1113293, 1154457) and the Australian Research Council, Australia (CE140100011). Â.F.C., S.M., J.L.G., M.I.M., R.M.R., and K.S. were supported by Fundação para a Ciência e a Tecnologia, Portugal (DL57/2016/CP1451/CT0004, DL57/2016/CP1451/CT0010, PD/BD/139053/2018, PD/BD/135454/2017, PTDC/MAT-APL/31602/2017, and CEECIND/00697/2018, respectively), P.L. was supported by Conselho Nacional de Desenvolvimento Científico e Tenológico, Brazil (SN/CGEFO/CNPQ 201801/2015-9), and A.T.T. was supported in part by Alfred P. Sloan Foundation Fellowship (FG-2020-12949).

AUTHOR CONTRIBUTIONS

Conceptualization, Â.F.C. and M.M.M.; methodology, Â.F.C.; investigation, Â.F.C., S.M., J.L.G., P.L., D.F.-R., M.I.M., D.G.d.C., P.R., and T.C.; software, A.T.T.; formal analysis, Â.F.C. and R.M.R.; resources, K.S., W.R.H., and B.S.-S.; writing – original draft, Â.F.C. and M.M.M.; writing – review & editing, Â.F.C., B.S.-S., and M.M.M.; visualization, Â.F.C.; funding acquisition, Â.F.C. and M.M.M.

DECLARATION OF INTERESTS

The authors declare no competing interests.

Received: April 29, 2022
Revised: November 10, 2022
Accepted: January 26, 2023
Published: February 17, 2023

REFERENCES

1. Langhorne, J., Ndungu, F.M., Sponaas, A.M., and Marsh, K. (2008). Immunity to malaria: more questions than answers. Nat. Immunol. *9*, 725–732. https://doi.org/10.1038/ni.f.205.
2. Haldar, K., Murphy, S.C., Milner, D.A., and Taylor, T.E. (2007). Malaria: mechanisms of erythrocytic infection and pathological correlates of severe disease. Annu. Rev. Pathol. *2*, 217–249. https://doi.org/10.1146/annurev.pathol.2.010506.091913.
3. Miller, J.L., Sack, B.K., Baldwin, M., Vaughan, A.M., and Kappe, S.H.I. (2014). Interferon-mediated innate immune responses against malaria parasite liver stages. Cell Rep. *7*, 436–447. https://doi.org/10.1016/j.celrep.2014.03.018.
4. Liehl, P., Zuzarte-Luís, V., Chan, J., Zillinger, T., Baptista, F., Carapau, D., Konert, M., Hanson, K.K., Carret, C., Lassnig, C., et al. (2014). Host-cell sensors for Plasmodium activate innate immunity against liver-stage infection. Nat. Med. *20*, 47–53.
5. Spence, P.J., Jarra, W., Lévy, P., Reid, A.J., Chappell, L., Brugat, T., Sanders, M., Berriman, M., and Langhorne, J. (2013). Vector transmission regulates immune control of Plasmodium virulence. Nature *498*, 228–231. https://doi.org/10.1038/nature12231.
6. Doolan, D.L., Dobaño, C., and Baird, J.K. (2009). Acquired immunity to Malaria. Clin. Microbiol. Rev. *22*, 13–36. https://doi.org/10.1128/CMR.00025-08.
7. Georgiadou, A., Lee, H.J., Walther, M., van Beek, A.E., Fitriani, F., Wouters, D., Kuijpers, T.W., Nwakanma, D., D'Alessandro, U., Riley, E.M., et al. (2019). Modelling pathogen load dynamics to elucidate mechanistic determinants of host–Plasmodium falciparum interactions. Nat. Microbiol. *4*, 1592–1602. https://doi.org/10.1038/s41564-019-0474-x.
8. Pamplona, A., Ferreira, A., Balla, J., Jeney, V., Balla, G., Epiphanio, S., Chora, A., Rodrigues, C.D., Gregoire, I.P., Cunha-Rodrigues, M., et al. (2007). Heme oxygenase-1 and carbon monoxide suppress the pathogenesis of experimental cerebral malaria. Nat. Med. *13*, 703–710. https://doi.org/10.1038/nm1586.
9. Hee, L., Dinudom, A., Mitchell, A.J., Grau, G.E., Cook, D.I., Hunt, N.H., and Ball, H.J. (2011). Reduced activity of the epithelial sodium channel in malaria-induced pulmonary oedema in mice. Int. J. Parasitol. *41*, 81–88. https://doi.org/10.1016/j.ijpara.2010.07.013.
10. Mukherjee, D., Chora, Â.F., Lone, J.C., Ramiro, R.S., Blankenhaus, B., Serre, K., Ramirez, M., Gordo, I., Veldhoen, M., Varga-Weisz, P., et al. (2022). Host lung microbiota promotes malaria-associated acute respiratory distress syndrome. Nat. Commun. *13*, 3747. https://doi.org/10.1038/s41467-022-31301-8.
11. Robert, V., Macintyre, K., Keating, J., Trape, J.F., Duchemin, J.B., Warren, M., and Beier, J.C. (2003). Malaria transmission in urban sub-Saharan Africa. Am. J. Trop. Med. Hyg. *68*, 169–176. https://doi.org/10.4269/ajtmh.2003.68.169.
12. Portugal, S., Carret, C., Recker, M., Armitage, A.E., Gonçalves, L.A., Epiphanio, S., Sullivan, D., Roy, C., Newbold, C.I., Drakesmith, H., et al. (2011). Host-mediated regulation of superinfection in malaria. Nat. Med. *17*, 732–737.
13. Rosenberg, R., Wirtz, R.A., Schneider, I., and Burge, R. (1990). An estimation of the number of malaria sporozoites ejected by a feeding mosquito. Trans. R. Soc. Trop. Med. Hyg. *84*, 209–212. https://doi.org/10.1016/0035-9203(90)90258-G.
14. Amino, R., Thiberge, S., Martin, B., Celli, S., Shorte, S., Frischknecht, F., and Ménard, R. (2006). Quantitative imaging of Plasmodium transmission from mosquito to mammal. Nat. Med. *12*, 220–224. https://doi.org/10.1038/nm1350.
15. Filipe, J.A.N., Riley, E.M., Drakeley, C.J., Sutherland, C.J., and Ghani, A.C. (2007). Determination of the processes driving the acquisition of immunity to malaria using a mathematical transmission model. PLoS Comp. Biol. *3*, e255. https://doi.org/10.1371/journal.pcbi.0030255.
16. Gupta, S., Snow, R.W., Donnelly, C.A., Marsh, K., and Newbold, C. (1999). Immunity to non-cerebral severe malaria is acquired after one or two infections. Nat. Med. *5*, 340–343.
17. Sebina, I., and Haque, A. (2018). Effects of type I interferons in malaria. Immunology *155*, 176–185. https://doi.org/10.1111/imm.12971.
18. Pais, T.F., Ali, H., Moreira da Silva, J., Duarte, N., Neres, R., Chhatbar, C., Acúrcio, R.C., Guedes, R.C., Strano Moraes, M.C., Costa-Silva, B., et al. (2022). Brain endothelial STING1 activation by Plasmodium -sequestered

heme promotes cerebral malaria via type I IFN response. Proc. Natl. Acad. Sci. USA *119*. e2206327119. https://doi.org/10.1073/pnas.2206327119.

19. Barrera, V., Haley, M.J., Strangward, P., Attree, E., Kamiza, S., Seydel, K.B., Taylor, T.E., Milner, D.A., Craig, A.G., and Couper, K.N. (2019). Comparison of CD8+ T cell accumulation in the brain during human and murine cerebral malaria. Front. Immunol. *10*, 1747. https://doi.org/10.3389/fimmu.2019.01747.
20. Ghazanfari, N., Mueller, S.N., and Heath, W.R. (2018). Cerebral malaria in mouse and man. Front. Immunol. *9*, 2016. https://doi.org/10.3389/fimmu.2018.02016.
21. Riggle, B.A., Manglani, M., Maric, D., Johnson, K.R., Lee, M.H., Neto, O.L.A., Taylor, T.E., Seydel, K.B., Nath, A., Miller, L.H., et al. (2020). CD8+ T cells target cerebrovasculature in children with cerebral malaria. J. Clin. Invest. *130*, 1128–1138. https://doi.org/10.1172/JCI133474.
22. Fernandes, P., Howland, S.W., Heiss, K., Hoffmann, A., Hernández-Castañeda, M.A., Obrová, K., Frank, R., Wiedemann, P., Bendzus, M., Rénia, L., et al. (2018). A plasmodium cross-stage antigen contributes to the development of experimental cerebral malaria. Front. Immunol. *9*, 1875. https://doi.org/10.3389/fimmu.2018.01875.
23. Lau, L.S., Fernandez-Ruiz, D., Mollard, V., Sturm, A., Neller, M.A., Cozijnsen, A., Gregory, J.L., Davey, G.M., Jones, C.M., Lin, Y.H., et al. (2014). CD8+ T cells from a novel T cell receptor transgenic mouse induce liver-stage immunity that can be boosted by blood-stage infection in rodent malaria. PLoS Pathog. *10*, e1004135. https://doi.org/10.1371/journal.ppat.1004135.
24. Müller, K., Gibbins, M.P., Matuschewski, K., and Hafalla, J.C.R. (2017). Evidence of cross-stage CD8+ T cell epitopes in malaria pre-erythrocytic and blood stage infections. Parasite Immunol. *39*, e12434. https://doi.org/10.1111/pim.12434.
25. Valencia-Hernandez, A.M., Ng, W.Y., Ghazanfari, N., Ghilas, S., de Menezes, M.N., Holz, L.E., Huang, C., English, K., Naung, M., Tan, P.S., et al. (2020). A natural peptide antigen within the plasmodium ribosomal protein RPL6 confers liver TRM cell-mediated immunity against malaria in mice. Cell Host Microbe *27*, 950–962.e7. https://doi.org/10.1016/j.chom.2020.04.010.
26. Ribot, J.C., Neres, R., Zuzarte-Luís, V., Gomes, A.Q., Mancio-Silva, L., Mensurado, S., Pinto-Neves, D., Santos, M.M., Carvalho, T., Landry, J.J.M., et al. (2019). γδ-T cells promote IFN-γ–dependent Plasmodium pathogenesis upon liver-stage infection. Proc. Natl. Acad. Sci. USA *116*, 9979–9988. https://doi.org/10.1073/pnas.1814440116.
27. Zaidi, I., Diallo, H., Conteh, S., Robbins, Y., Kolasny, J., Orr-Gonzalez, S., Carter, D., Butler, B., Lambert, L., Brickley, E., et al. (2017). γδ T cells Are Required for the Induction of Sterile Immunity during Irradiated Sporozoite Vaccinations. J. Immunol. *199*, 3781–3788. https://doi.org/10.4049/jimmunol.1700314.
28. Soares, M.P., Teixeira, L., and Moita, L.F. (2017). Disease tolerance and immunity in host protection against infection. Nat. Rev. Immunol. *17*, 83–96. https://doi.org/10.1038/nri.2016.136.
29. Ribot, J.C., deBarros, A., Pang, D.J., Neves, J.F., Peperzak, V., Roberts, S.J., Girardi, M., Borst, J., Hayday, A.C., Pennington, D.J., et al. (2009). CD27 is a thymic determinant of the balance between interferon-γ- and interleukin 17-producing γδ T cell subsets. Nat. Immunol. *10*, 427–436. https://doi.org/10.1038/ni.1717.
30. Muñoz-Ruiz, M., Sumaria, N., Pennington, D.J., and Silva-Santos, B. (2017). Thymic Determinants of γδ T cell Differentiation. Trends Immunol. *38*, 336–344. https://doi.org/10.1016/j.it.2017.01.007.
31. Muñoz-Ruiz, M., Ribot, J.C., Grosso, A.R., Gonçalves-Sousa, N., Pamplona, A., Pennington, D.J., Regueiro, J.R., Fernández-Malavé, E., and Silva-Santos, B. (2016). TCR signal strength controls thymic differentiation of discrete proinflammatory γδT cell subsets. Nat. Immunol. *17*, 721–727. https://doi.org/10.1038/ni.3424.
32. Ribot, J.C., Chaves-Ferreira, M., d'Orey, F., Wencker, M., Gonçalves-Sousa, N., Decalf, J., Simas, J.P., Hayday, A.C., and Silva-Santos, B. (2010). Cutting Edge: adaptive versus Innate Receptor Signals Selectively Control the Pool Sizes of Murine IFN-γ– or IL-17–Producing γδ T cells upon Infection. J. Immunol. *185*, 6421–6425. https://doi.org/10.4049/jimmunol.1002283.
33. Behr, C., Poupot, R., Peyrat, M.A., Poquet, Y., Constant, P., Dubois, P., Bonneville, M., and Fournie, J.J. (1996). Plasmodium falciparum stimuli for human γδ T cells are related to phosphorylated antigens of mycobacteria. Infect. Immun. *64*, 2892–2896. https://doi.org/10.1128/iai.64.8.2892-2896.1996.
34. Morita, C.T., Jin, C., Sarikonda, G., and Wang, H. (2007). Nonpeptide antigens, presentation mechanisms, and immunological memory of human Vγ2Vδ2 T cells: discriminating friend from foe through the recognition of prenyl pyrophosphate antigens. Immunol. Rev. *215*, 59–76. https://doi.org/10.1111/j.1600-065X.2006.00479.x.
35. Jagannathan, P., Kim, C.C., Greenhouse, B., Nankya, F., Bowen, K., Eccles-James, I., Muhindo, M.K., Arinaitwe, E., Tappero, J.W., Kamya, M.R., et al. (2014). Loss and dysfunction of Vδ2+γδ T cells are associated with clinical tolerance to malaria. Sci. Transl. Med. *6*, 251ra117. https://doi.org/10.1126/scitranslmed.3009793.
36. Farrington, L.A., Jagannathan, P., McIntyre, T.I., Vance, H.M., Bowen, K., Boyle, M.J., Nankya, F., Wamala, S., Auma, A., Nalubega, M., et al. (2016). Frequent malaria drives progressive Vδ2 T-cell loss, dysfunction, and CD16 up-regulation during early childhood. J. Infect. Dis. *213*, 1483–1490. https://doi.org/10.1093/infdis/jiv600.
37. Jagannathan, P., Lutwama, F., Boyle, M.J., Nankya, F., Farrington, L.A., McIntyre, T.I., Bowen, K., Naluwu, K., Nalubega, M., Musinguzi, K., et al. (2017). Vδ2+ T cell response to malaria correlates with protection from infection but is attenuated with repeated exposure. Sci. Rep. *7*, 11487. https://doi.org/10.1038/s41598-017-10624-3.
38. Sandrock, I., Reinhardt, A., Ravens, S., Binz, C., Wilharm, A., Martins, J., Oberdörfer, L., Tan, L., Lienenklaus, S., Zhang, B., et al. (2018). Genetic models reveal origin, persistence and nonredundant functions of IL-17-producing γδ T cells. J. Exp. Med. *215*, 3006–3018. https://doi.org/10.1084/jem.20181439.
39. Kim, T.S., Hanak, M., Trampont, P.C., and Braciale, T.J. (2015). Stress-associated erythropoiesis initiation is regulated by type 1 conventional dendritic cells. J. Clin. Invest. *125*, 3965–3980. https://doi.org/10.1172/JCI81919.
40. Cromer, D., Evans, K.J., Schofield, L., and Davenport, M.P. (2006). Preferential invasion of reticulocytes during late-stage plasmodium berghei infection accounts for reduced circulating reticulocyte levels. Int. J. Parasitol. *36*, 1389–1397. https://doi.org/10.1016/j.ijpara.2006.07.009.
41. Malleret, B., Li, A., Zhang, R., Tan, K.S.W., Suwanarusk, R., Claser, C., Cho, J.S., Koh, E.G.L., Chu, C.S., Pukrittayakamee, S., et al. (2015). Plasmodium vivax: restricted tropism and rapid remodeling of CD71-positive reticulocytes. Blood *125*, 1314–1324. https://doi.org/10.1182/blood-2014-08-596015.
42. Miller, L.H., Ackerman, H.C., Su, X.Z., and Wellems, T.E. (2013). Malaria biology and disease pathogenesis: insights for new treatments. Nat. Med. *19*, 156–167. https://doi.org/10.1038/nm.3073.
43. Hanson, J., Lam, S.W.K., Mahanta, K.C., Pattnaik, R., Alam, S., Mohanty, S., Hasan, M.U., Hossain, A., Charunwatthana, P., Chotivanich, K., et al. (2012). Relative contributions of macrovascular and microvascular dysfunction to disease severity in falciparum malaria. J. Infect. Dis. *206*, 571–579. https://doi.org/10.1093/infdis/jis400.
44. Alkema, M., Yap, X.Z., de Jong, G.M., Reuling, I.J., de Mast, Q., van Crevel, R., Ockenhouse, C.F., Collins, K.A., Bousema, T., McCall, M.B.B., et al. (2022). Controlled human malaria infections by mosquito bites induce more severe clinical symptoms than asexual blood-stage challenge infections. EBioMedicine *77*, 103919. https://doi.org/10.1016/j.ebiom.2022.103919.
45. Sato, Y., Ries, S., Stenzel, W., Fillatreau, S., and Matuschewski, K. (2019). The liver-stage plasmodium infection is a critical checkpoint for development of experimental cerebral malaria. Front. Immunol. *10*, 2554. https://doi.org/10.3389/fimmu.2019.02554.
46. Casals-Pascual, C., Idro, R., Gicheru, N., Gwer, S., Kitsao, B., Gitau, E., Mwakesi, R., Roberts, D.J., and Newton, C.R.J.C. (2008). High levels of

erythropoietin are associated with protection against neurological sequelae in African children with cerebral malaria. Proc. Natl. Acad. Sci. USA *105*, 2634–2639. https://doi.org/10.1073/pnas.0709715105.

47. Kaiser, K., Texier, A., Ferrandiz, J., Buguet, A., Meiller, A., Latour, C., Peyron, F., Cespuglio, R., and Picot, S. (2006). Recombinant human erythropoietin prevents the death of mice during cerebral malaria. J. Infect. Dis. *193*, 987–995. https://doi.org/10.1086/500844.

48. Wiese, L., Hempel, C., Penkowa, M., Kirkby, N., and Kurtzhals, J.A.L. (2008). Recombinant human erythropoietin increases survival and reduces neuronal apoptosis in a murine model of cerebral malaria. Malar. J. *7*, 3. https://doi.org/10.1186/1475-2875-7-3.

49. Wei, X., Li, Y., Sun, X., Zhu, X., Feng, Y., Liu, J., Jiang, Y., Shang, H., Cui, L., and Cao, Y. (2014). Erythropoietin protects against murine cerebral malaria through actions on host cellular immunity. Infect. Immun. *82*, 165–173. https://doi.org/10.1128/IAI.00929-13.

50. Picot, S., Bienvenu, A.L., Konate, S., Sissoko, S., Barry, A., Diarra, E., Bamba, K., Djimdé, A., and Doumbo, O.K. (2009). Safety of epoietin beta-quinine drug combination in children with cerebral malaria in Mali. Malar. J. *8*, 169. https://doi.org/10.1186/1475-2875-8-169.

51. Marquet, S., Conte, I., Poudiougou, B., Argiro, L., Cabantous, S., Dessein, H., Burté, F., Oumar, A.A., Brown, B.J., Traore, A., et al. (2016). The IL17F and IL17RA genetic variants increase risk of cerebral malaria in two African populations. Infect Immun. *84*, 590–597. https://doi.org/10.1128/IAI.00671-15.

52. Papotto, P.H., Ribot, J.C., and Silva-Santos, B. (2017). IL-17+ γδ T cells as kick-starters of inflammation. Nat. Immunol. *18*, 604–611. https://doi.org/10.1038/ni.3726.

53. Ribot, J.C., Lopes, N., and Silva-Santos, B. (2021). γδ T cells in tissue physiology and surveillance. Nat. Rev. Immunol. *21*, 221–232. https://doi.org/10.1038/s41577-020-00452-4.

54. Reinhardt, R.L., Liang, H.E., Bao, K., Price, A.E., Mohrs, M., Kelly, B.L., and Locksley, R.M. (2015). A novel model for IFN-γ–mediated autoinflammatory syndromes. J. Immunol. *194*, 2358–2368. https://doi.org/10.4049/jimmunol.1401992.

55. Franke-Fayard, B., Trueman, H., Ramesar, J., Mendoza, J., Van Der Keur, M., Van Der Linden, R., Sinden, R.E., Waters, A.P., and Janse, C.J. (2004). A Plasmodium berghei reference line that constitutively expresses GFP at a high level throughout the complete life cycle. Mol. Biochem. Parasitol. *137*, 23–33. https://doi.org/10.1016/j.molbiopara.2004.04.007.

56. Nakae, S., Komiyama, Y., Nambu, A., Sudo, K., Iwase, M., Homma, I., Sekikawa, K., Asano, M., and Iwakura, Y. (2002). Antigen-specific T cell sensitization is impaired in IL-17-deficient mice, causing suppression of allergic cellular and humoral responses. Immunity *17*, 375–387. https://doi.org/10.1016/S1074-7613(02)00391-6.

57. Haks, M.C., Krimpenfort, P., Borst, J., and Kruisbeek, A.M. (1998). The CD3gamma chain is essential for development of both the TCRalphabeta and TCRgammadelta lineages. EMBO J. *17*, 1871–1882.

58. Dave, V.P., Cao, Z., Browne, C., Alarcon, B., Fernandez-Miguel, G., Lafaille, J., de la Hera, A., Tonegawa, S., and Kappes, D.J. (1997). CD3d deficiency arrests development of the ab but not the gd T cell lineage. EMBO J. *16*, 1360–1370.

59. M'Bana, V., Lahree, A., Marques, S., Slavic, K., and Mota, M.M. (2022). Plasmodium parasitophorous vacuole membrane-resident protein UIS4 manipulates host cell actin to avoid parasite elimination. iScience *25*, 104281. https://doi.org/10.1016/j.isci.2022.104281.

60. Kumar, H., Sattler, J.M., Singer, M., Heiss, K., Reinig, M., Hammerschmidt-Kamper, C., Heussler, V., Mueller, A.K., and Frischknecht, F. (2016). Protective efficacy and safety of liver stage attenuated malaria parasites. Sci. Rep. *6*, 26824. https://doi.org/10.1038/srep26824.

61. Gundersen, H.J.G., and Jensen, E.B. (1987). The efficiency of systematic sampling in stereology and its prediction. J. Microsc. *147*, 229–263. https://doi.org/10.1111/j.1365-2818.1987.tb02837.x.

62. Tschanz, S.A., Burri, P.H., and Weibel, E.R. (2011). A simple tool for stereological assessment of digital images: the STEPanizer. J. Microsc. *243*, 47–59. https://doi.org/10.1111/j.1365-2818.2010.03481.x.

63. Yates, A., Callard, R., and Stark, J. (2004). Combining cytokine signalling with T-bet and GATA-3 regulation in Th1 and Th2 differentiation: A model for cellular decision-making. J. Theor. Biol. *231*, 181–196. https://doi.org/10.1016/j.jtbi.2004.06.013.

STAR★METHODS

KEY RESOURCES TABLE

REAGENT or RESOURCE	SOURCE	IDENTIFIER
Antibodies		
Unconjugated anti-mouse CD16/CD32, clone 93	eBiosciences	Cat# 14-0161-82; RRID: AB_467133
PerCP anti-mouse CD3, clone 145-2C11	Biolegend	Cat# 100325; RRID: AB_893319
Brilliant Violet 710 anti-mouse CD3, clone 145-2C11	Biolegend	Cat# 100349; RRID: AB_2565841
APC-Cy7 anti-mouse CD4, clone GK1.5	Biolegend	Cat# 100413; RRID: AB_312698
APC-Cy7 anti-mouse CD4, clone RM4-5	Biolegend	Cat# 100525; RRID: AB_312726
PE-Cy7 anti-mouse CD8a, clone 53-6.7	Biolegend	Cat# 100722; RRID: AB_312761
FITC anti-mouse/human CD11b, clone	Biolegend	Cat# 101205; RRID: AB_312788
PE anti-mouse TCRγ/δ, clone GL3	Biolegend	Cat# 118107; RRID: AB_313831
PE-Cy7 anti-mouse Vγ4 (Vγ2 in the Garman nomenclature), clone UC3-10A6	eBiosciences	Cat# 25-5828-82; RRID: AB_2573474
APC anti-mouse TCR Vγ1.1, clone 2.11	Biolegend	Cat# 141107; RRID: AB_10897806
Brilliant Violet 605 anti-mouse/human CD44, clone IM7	Biolegend	Cat# 103047; RRID: AB_2562451
Brilliant Violet 510 anti-mouse CD45, clone 30-F11	Biolegend	Cat# 103137; RRID: AB_2561392
APC anti-mouse CD45, clone 30-F11	Biolegend	Cat# 103111; RRID: AB_312976
PE anti-mouse CD71, clone RI7217	Biolegend	Cat# 113807; RRID: AB_313568
PerCP-Cy5.5 anti-mouse Ter-119, clone TER-119	eBiosciences	Cat# 45-5921-82; RRID: AB_925765
APC-Cy7 anti-mouse Ter-119, clone TER-119	Biolegend	Cat# 116223; RRID: AB_2137788
Brilliant Violet 711 anti-mouse IFN-γ, clone XMG1.2	Biolegend	Cat# 505835; RRID: AB_11219588
PE anti-mouse IFN-γ, clone XMG1.2	Biolegend	Cat# 505808; RRID: AB_315402
PE-Cy7 anti-human/mouse Granzyme B, clone QA16A02	Biolegend	Cat# 372214; RRID: AB_2728381
APC-Cy7 anti-mouse IL-17A, clone TC11-18H10.1	Biolegend	Cat# 506939; RRID: AB_2565780
*InVivo*MAb anti-mouse CD24, clone M1/69	BioXCell	Cat# BE0360; RRID: AB_2894779
*InVivo*Plus rat IgG2b isotype control, Clone LTF-2	BioXCell	Cat# BP0090; RRID: AB_1107780
***Plasmodium* parasite strains**		
Plasmodium berghei ANKA wild-type	Propagated in house[54]	N/A
Plasmodium berghei ANKA *uis4*$^-$	Propagated in house[23]	N/A
Plasmodium berghei ANKA *lisp2*$^-$	Provided by F. Frischknecht[55] and propagated in house	N/A
Plasmodium berghei K173	Propagated in house[9]	N/A
Chemicals, peptides, and recombinant proteins		
Hoechst 33342, Trihydrochloride, Trihydrate	Invitrogen	Cat# H1399
DNase I recombinant, RNase-free	Roche	Cat# 04716728001

(*Continued on next page*)

Continued

REAGENT or RESOURCE	SOURCE	IDENTIFIER
Collagenase from *Clostridium histolyticum*, type VIII	Sigma-Aldrich	Cat# C2139
Percoll®	Sigma-Aldrich	Cat# P1644
Percoll®	Sigma-Aldrich	Cat# GE17-0891-01
Phenylhydrazine hydrochloride	Sigma-Aldrich	Cat# 114715
IVISbrite D-Luciferin Potassium Salt Bioluminescent Substrate (XenoLight)	PerkinElmer	Cat# 122799
Brefeldin A from Eupenicillium brefeldianum	Calbiochem	Cat# 203729
Phorbol 12-myristate 13-acetate (PMA)	Merck	Cat# P8139
Ionomycin calcium salt from Streptomyces conglobatus	Calbiochem	Cat# 407952
PureZOL™ RNA Isolation Reagent	Bio Rad	Cat# 7326890
Critical commercial assays		
NZY Total RNA Isolation kit	NZYtech	Cat# MB13402
One-step NZYSpeedy RT-qPCR Probe kit, ROX plus	NZYtech	Cat# MB350
LIVE/DEAD™ Fixable Violet Dead Cell Stain Kit	ThermoFisher	Cat# L34963
$CD8a^+$ T Cell Isolation Kit, mouse	Miltenyi Biotec	Cat# 130-104-075
Deposited data		
Raw and analyzed data	This paper	Mendeley Data: https://doi.org/10.17632/8v5y93rpxk.1
Experimental models: Organisms/strains		
Mouse: C57BL/6J mice	Charles Rivers Laboratories	CRL Code #632; RRID: IMSR_JAX:000664
Mouse: Transgenic PbT-I mice	Provided by W. Heath[56] and bread at Department of Microbiology and Immunology, The University of Melbourne, Australia.	N/A
Mouse: *Tcrδ*$^{-/-}$: B6.129P2-Tcrd^{tm1Mom}/J	Jackson Laboratory and bread at iMM-JLA.	JAX stock #002120; RRID:IMSR_JAX:002120
Mouse: *Cd3*γ$^{-/-}$	Provided by D. Kappes[52] and bred at iMM-JLA.	N/A
Mouse: *Cd3*δ$^{-/-}$	Provided by I. Luescher[53] and bred at iMM-JLA.	N/A
Mouse: *Il-17*$^{-/-}$	Provided by F. Powrie with permission from Y. Iwakura[57] and bred at iMM-JLA.	N/A
Mouse: Great: B6.129S4-*Ifng*$^{tm3.1Lky}$/J	Provided by M. Mohrs[58] and bred at iMM-JLA.	JAX Stock #017581; RRID:IMSR_JAX:017581
Mouse: *Tcrδ*-GDL:	Provided by I. Prinz[38] and bred at iMM-JLA.	N/A
Mouse: *Ifnar1*$^{-/-}$:	Bred at Instituto Gulbenkian de Ciência	N/A
Oligonucleotides		
Primer: *P. berghei 18s* gene - Forward: AGGGAGCCTGAGAAATAG	This paper	N/A
Primer: *P. berghei 18s* gene - Reverse: GTCACTACCTCTCTTATTTAGAA	This paper	N/A
Probe: *P. berghei 18s* gene – 6-FAM-ACCACATCTAAGGAAGGCAGCA-BHQ1	This paper	N/A
Primer: *M. musculus hypoxanthine-guanine phosphoribosyltransferase* (Hprt) gene–Forward: GAACCAGGTTATGACCTA	This paper	N/A
Primer: *M. musculus hypoxanthine-guanine phosphoribosyltransferase* (Hprt) gene–Reverse: TCTCCTTCATGACATCTC	This paper	N/A

(*Continued on next page*)

Continued

REAGENT or RESOURCE	SOURCE	IDENTIFIER
Probe: *M. musculus hypoxanthine-guanine phosphoribosyltransferase* (Hprt) gene– 6-FAM-TTCAGTCCTGTCCATAATCAGTCCAT-BHQ1	This paper	N/A
Software and algorithms		
NDP.view2 Image	Hamamatsu; https://www.hamamatsu.com/eu/en/product/life-science-and-medical-systems/digital-slide-scanner/U12388-01.html	Cat# U12388-01
STEPanizer	https://www.stepanizer.com/	N/A
Living Image V3.0	PerkinElmer	N/A
FlowJo V10.7.1	Tree Star Inc.; https://www.flowjo.com/	RRID:SCR_008520
Prism V8.4.3	Graphpad; https://www.graphpad.com/scientific-software/prism/	RRID:SCR_002798
NLME package of R V3.1-155	http://cran.r-project.org/	N/A
Illustrator CS6	Adobe; https://www.adobe.com/pt/products/illustrator.html	RRID: SCR_010279

RESOURCE AVAILABILITY

Lead contact

Further information and requests for resources and reagents should be directed to and will be fulfilled by the lead contact, Maria M. Mota (mmota@medicina.ulisboa.pt).

Materials availability

This study did not generate new unique reagents.

Data and code availability

All data is available in the main text or in the supplemental information and can be assessed at Mendeley Data: https://doi.org/10.17632/8v5y93rpxk.1. The original code for the mathematical models is available at Mendeley Data: https://doi.org/10.17632/f3sfsw7vn2.1. Any additional information required to reanalyze the data reported in this paper is available from the lead contact upon request.

EXPERIMENTAL MODEL AND SUBJECT DETAILS

Mice

C57BL/6J wild-type mice were obtained from Charles River Laboratories International Inc. Tcr delta-deficient mice (*Tcrδ*$^{-/-}$; originally obtained from The Jackson Laboratory), CD3γ and CD3δ double-haploinsufficient mice (CD3DH, *Cd3γ*$^{+/-}$ *Cd3δ*$^{+/-}$; obtained by crossing *Cd3γ*$^{-/-}$ males (originally obtained from D. Kappes, Fox Chase Cancer Center, Philadelphia[57]) with *Cd3δ*$^{-/-}$ females (originally obtained from I. Luescher, Ludwig Institute for Cancer Research, Lausanne[58]), *Il-17*-deficient mice (*Il-17*$^{-/-}$; originally obtained from F. Powrie, University of Oxford, Oxford, with permission from Y. Iwakura, Tokyo University of Science, Chiba, Japan),[56] Great mice (IFN-γ reporter with endogenous polyA tail, originally obtained from M. Mohrs, Trudeau Institute, NY),[54] and *Tcr*δ-GDL mice (expressing GFP, human Diphtheria Toxin (DTx) receptor, and luciferase under the control of an internal ribosome entry site (IRES) in the 3′UTR of the *Tcr*δ gene, originally obtained from I. Prinz, Hannover Medical School, Hannover[38]) were bred at the Instituto de Medicina Molecular – João Lobo Antunes (iMM-JLA), Lisbon, Portugal. Type 1 IFN receptor subunit 1-deficient mice (*Ifnar1*$^{-/-}$) were obtained from IGC, Oeiras. PbT-1 transgenic mice[23] were bred at the Department of Microbiology and Immunology, The University of Melbourne, Australia. All genetically-modified mouse strains used are in the C57BL/6J genetic background and have been backcrossed at least ten times. All mice were maintained in specific pathogen–free conditions. For the studies, both males and females (6-10 weeks old) were used. Animal experimentation protocols were approved by the institutional animal welfare body – ORBEA-iMM-JLA – and by the Direcção-Geral de Alimentação e Veterinária (Portugal), and by the Melbourne Health Research Animal Ethics Committee, University of Melbourne (Australia). All procedures were performed in strict accordance with the Directive 2010/63/EU and the Australian code of practice for the care and use of animals for scientific purposes.

Parasites

GFP-expressing *P. berghei* ANKA (PbANKA) wild-type,[55] *uis4*$^{-}$ (upregulated in infective sporozoites gene 4)[59] and *lisp2*$^{-}$ (liver-specific protein 2)[60] sporozoites were obtained by dissection of the salivary glands of infected *Anopheles stephensi* mosquitoes bred at the

iMM-JLA (Lisbon). Fresh RBCs infected with either PbANKA or *P. berghei* K173 (PbK173)[9] parasites to seed BS infections with the designated inocula were obtained from a passage mouse, 4 days after injection via intraperitoneal route with 10^7 crio-preserved iRBCs from each parasite line.

METHOD DETAILS

Infections

For LS+BS infections, mice were injected, via retro-orbital route, with the designated quantity of radiation-attenuated (16,000 rads; Caesium^{137} γ-source, Gammacell® 3000 Elan, Theratronics) or genetically-attenuated sporozoites in 200μl of DMEM medium. Heat-killed sporozoites (15 minutes at 72°C followed by 15 minutes at 95°C) were injected into mice at the indicated quantities using the same volume and administration route. BS-infected controls received equivalent amounts of salivary glands extract from uninfected *Anopheles stephensi* mosquitoes using the same volume and administration route. At the designated times after sporozoite administration, mice received the designated quantity of fresh WT GFP-expressing PbANKA or PbK173 infected RBCs in 200μl of PBS via intraperitoneal or retro-orbital routes. For live sporozoite infections, mice were injected, via retro-orbital route, with the designated quantity of sporozoites in 200μl of DMEM medium. Parasitemia (expressed as percentage of iRBCs) was monitored daily either directly (GFP-expressing PbANKA) or following DNA staining using Hoescht 33342 (4,4μg/mL; Invitrogen) to detect parasitized Ter119$^+$ CD45$^-$ RBCs (PbK173) by fluorescence activated cell sorting (FACS) on a Fortessa analyzer (BD Biosciences) using FlowJo-V10 software (Tree Star Inc.).

ECM assessment

Mice survival was monitored twice daily from day 4 post infection onwards. ECM onset was evaluated by the development of neurological symptoms (ataxia and paralysis), assessed as the inability of mice to self-right.

Histopathology and Stereology

Mice were euthanized with CO_2 narcosis, necropsy was performed and lung and/or CNS (brain, cerebellum and spinal cord) were collected and fixed in formalin. Brains were collected after overt ECM (BS^{low} at day 8 p.i.; BS^{high} at day 7 p.i.; LS+BS^{high} at day 6 p.i.), except for LS+BS^{low} group (day 8 p.i.). Lungs were collected after overt MA-ARDS (days 7-8 p.i. for all groups) except for LS+BS^{low} group (day 8 p.i.).

For pulmonary pathology, in addition to quantifying the volume of pleural effusion (fluid in the thoracic cavity), lung was paraffin-embedded, sectioned at 4μm, stained with Hematoxylin and Eosin and sections were analyzed by a pathologist blinded to experimental groups, in a Leica DM2000 microscope coupled to a Leica MC170 HD microscope camera (Leica Microsystems, Wetzlar, Germany). Pulmonary edema was scored according to 5-tier system with 0–4 grading scale (0, absent; 1, minimal; 2, mild; 3, moderate; 4, marked).

For brain pathology, stereology was used to measure brain volume and area (fraction) of cerebral hemorrhages. Briefly, after removal of the skull, brain was placed in a 1-mm mouse brain matrix, immersed in agarose and, once solidified, eight 2-mm thick coronal brain slices were obtained, placed into a cassette and processed for paraffin-embedding. 4μm sections were then stained with Hematoxylin and Eosin for assessment of brain volume; and with modified von Kossa stain (with omission of the silver nitrate step), for enhanced visualization of cerebral hemorrhages. Each section was digitally scanned in Nanozoomer SQ and visualized in NDP.view2 Image viewing software (Hamamatsu). Estimates of brain volume were obtained according to the Cavalieri method[61] using the STEPanizer software,[62] by using the formula V = T x a/p x $\sum$Pi, where T is the thickness between sections, Pi is the number of points hitting the brain and (a/p) is the area associated with each point. In order to measure the volume of intracerebral hemorrhage, a grid composed of squares (4x5mm) was superimposed on the slide thumbnail, on the screen. The sampling was randomly started from a corner of the slide that did not include tissue section. Then, the slide was moved in the X- and Y-directions at equal distances. A grid containing 296 points (+), the central one encircled (⊕), was superposed on the tissue displayed in the screen. Volume measurements were obtained as follows: (1) Brain: every time brain was hit by the encircled point (⊕); (2) Hemorrhage: every time hemorrhage was hit by a point (+). The fraction of intracerebral hemorrhage volume was obtained dividing the points hit by hemorrhagic foci by the points hit by brain:

$$VF = \frac{Pi(Hemorrhage)}{Pi(Brain)\ x\ 296}.$$

The hemorrhage volume was estimated from volume fraction: V (Hemorrhage) = VF x V(Brain).

PbT-1 CD8$^+$ T cell isolation and adoptive transfer

CD8$^+$ T cell were negatively enriched from the spleens and lymph nodes of GFP-expressing PbT-1 transgenic mice using CD8α$^+$ T Cell Isolation Kit (Miltenyi Biotec), according to the manufacturer's instructions. Twenty-four hours prior to infection, recipient mice received 50,000 purified GFP$^+$ PbT-1 cells, via intravenous route, in 200μl of HBSS buffer.

Isolation of tissue-infiltrating leukocytes

Mice were euthanized with CO2 narcosis at the indicated time points after infection, transcardially perfused with 15 mL of ice-cold PBS, and brains, livers, spleens and bone marrow cells were harvested. Brains were homogenized in HBSS (+ calcium, + magnesium; ThermoFisher) supplemented with collagenase VIII (0.2mg/mL; Sigma) and DNAse I (2U/mL; Roche) and incubated at 37°C for 30 minutes. Brain samples were then filtered through a 100 μm mesh and centrifuged. Livers and spleens were homogenized in PBS supplemented with DNAse I (2U/mL; Roche). Brain samples were resuspended in 30% isotonic Percoll (Sigma), whereas liver samples were resuspended in 35% isotonic Percoll. After centrifugation at 1360g for 20 minutes at room temperature, cell pellets were harvested and red blood cells were lysed. Bone marrow cells were isolated from femurs and tibiae by flushing with a 27G needle using RPMI (ThermoFisher) and homogenized by repeated pippeting. Spleen and bone marrow cell suspensions were centrifuged and analyzed before (erythroblasts) or following (leukocytes) red blood cells lysis. Total cell numbers were assessed in an Accuri™ C6 Plus analyzer (BD Biosciences), by acquiring a pre-established volume of each cell suspension.

Flow cytometry

Leukocytes, circulating reticulocytes and erythroblasts were immunophenotyped by labeling with monoclonal antibodies specific for CD3 (145-2C11), CD4 (GK1.5 or RM4-5), CD8 (53-6.7), CD11b (M1/70), TCRδ (GL3), Vγ1 (2.11), CD44 (IM7), CD45 (30-F11), CD71 (RI7217) (all Biolegend), Vγ4 (UC3-10A6) and Ter119 (TER-119) (eBioscience). Fc receptors were blocked using a monoclonal antibody specific for CD16/CD32 (93; eBioscience). Dead cells were excluded using a live/dead fixable dye (ThermoFisher). Production of cytokines was evaluated directly (IFN-γ production in γδ T cells isolated from Great transgenic mice) or following re-stimulation of isolated leukocytes by phorbol 12-myristate 13-acetate (PMA) (50ng/mL; Sigma) and ionomycin (500ng/mL; Calbiochem) for 4 hours at 37°C in the presence of brefeldin A (10μg/mL; Calbiochem). Cells were then surface labeled with antibodies and fixed with 2% paraformaldehyde. Intracellular staining was performed using monoclonal antibodies specific for IFN-γ (XMG1.2), IL-17 (TC11-18H10.1) or granzyme B (QA16A02) (all Biolegend) after cell permeabilization using saponin (5mg/mL; Sigma). Cells were analyzed on a Fortessa analyzer (BD Biosciences) using FlowJo-V10.7.1 software (Tree Star Inc.).

In vivo αCD24 antibody administration

Mice received 100μg of αCD24 mouse monoclonal antibody (M1/69; BioXCell) or isotype control IgG2b antibody (LTF-2; BioXCell) diluted in saline via intraperitoneal route, 4 hours after spz administration (natural and LS+BS^{low} infections) or 2 days prior to transfusion of iRBCs (BS^{low} infection).

Adoptive transfer of cells

CD71^{+} reticulocyte-enriched full blood was obtained from donor mice receiving three daily intraperitoneal injections of phenylhydrazyne (40 mg/kg of body weight; Sigma) diluted in PBS, 6 days after the first injection. RBC donor mice were injected with an equivalent volume of PBS in the same schedule. Recipient mice received 2x10^{8} CD71^{+} reticulocytes in 200μL of PBS from days 5 to 9 p.i. (LS+BS^{low} infections) or from days 7 to 11 p.i. (live spz infections) via retro-orbital route. Control recipients received equivalent amounts of RBC on the same schedule, using the same volume and administration route.

Real time bioluminescence imaging

Ex vivo spleen functional luciferase activity in γδ T cells was determined at the indicated time points after infection using an IVIS Lumina imaging system (PerkinElmer) and Living Image 3.0 software (PerkinElmer). Following light isofluorane anesthesia, mice received 200 μL D-luciferin (10mg/mL; PerkinElmer) dissolved in PBS via subcutaneous injection. After 9 minutes, animals were sacrificed, spleens were removed and bioluminescence images were acquired with a 12.5 cm field of view (FOV), medium binning factor, and an exposure time of 4 minutes. Quantitative analysis of bioluminescence was performed by measuring the luminescence signal radiance using the Living Image 3.0 software.

Splenectomy

Following anaesthesia (isoflurane 2-3%), mice received buprenorphine (1,5ug/ml) for pre-emptive analgesia and were prepared for surgery by shaving and desinfection of the dorsal left toracolumbar region. An incision was made left of the spine to open the skin and the abdominal cavity. The spleen was exposed, the splenic vessels isolated with an hemostat and cauterized. Vessels were cutted distal to the cauterized section and the spleen was removed. The abdomen and the skin were closed with sutures and surgical glue (3M Vetbond). Mice are monitored for pain and allowed to recover for one week before infection.

RNA isolation and quantitative reverse-transcriptase PCR

Total RNA was extracted from CNS tissue at the indicated time points after infection using PureZOL™ RNA Isolation Reagent (Bio Rad) and NZY Total RNA Isolation kit (NZYtech) according to the manufacturer's instructions, and quantified in a Nanodrop 1000 (Thermo Scientific). Primer/probe sets specific for *P. berghei 18s* gene (5′ primer: AGGGAGCCTGAGAAATAG; 3′ primer: GTCACTACCTCTCTTATTTAGAA; probe: 6-FAM-ACCACATCTAAGGAAGGCAGCA-BHQ1) and *Mus musculus hypoxanthine-guanine phosphoribosyltransferase* gene (*Hprt*) (5′ primer: GAACCAGGTTATGACCTA; 3′ primer: TCTCCTTCATGACATCTC; probe: 6-FAM-TTCAGTCCTGTCCATAATCAGTCCAT-BHQ1) were used. 100ng of total mRNA was used for tandem cDNA synthesis and amplification in an RT-PCR 7500 Fast cycler (Applied Biosystems) with One-step NZYSpeedy RT-qPCR Probe kit (NZYtech). The

protocol consisted of 1 cycle at 50°C for 20 minutes, 1 cycle at 95°C for 5 minutes followed by 40 cycles of 95°C for 5 seconds and 60°C for 1 minute. The parameter threshold cycle (Ct), corresponding to the point at which each amplification curve crosses the background level, was used to quantify the relative expression of *P. berghei 18s* gene with the comparative ΔCt method. *Hprt* served as the normalizing reference gene.

Within-host model

Parasite growth

Blood stage parasites **(B)** grow exponentially at rate r_P, with a logistic constraint governed by the carrying capacity K_B, which reflects a finite supply of red blood cells. Liver parasites **(L)** can suppress the proliferation of blood stage parasites through an independent, phenomenological mechanism (e.g. representing partially protective immunity or parasite competition) by reducing the carrying capacity for the blood stage parasites. Liver stage parasites can replicate exponentially at rate r_L, but this is inhibited by high blood stage densities. Liver stage parasites transition to blood stage parasites at rate t_r. Both stages have a natural mortality rate μ_i.

$$\frac{dL}{dt} = r_L L e^{-a_L B} - t_r L - \mu_L L \quad \text{(Equation 1)}$$

$$\frac{dB}{dt} = r_P B\left(1 - \left(\frac{B}{K_B e^{-a_B L} + B}\right)\right) + t_r L - \mu_P P \quad \text{(Equation 2)}$$

γδ T cell dynamics

In the absence of liver stage parasites, γδ T cells are not appreciably activated. However, in the presence of liver stage parasites, both γδ17 **(T_{17})** - and γδIFN **(T_N)** cells replicate in a liver stage density-dependent manner, as governed by a Hill function. K_L is the density of liver stages in which replication rates are half-maximum, and n_L is the coefficient that governs the steepness of the activation slope with respect to liver density. γδ T cell autoactivation and parasite density-dependent replication were structured similarly to the T_h cell polarization model first presented in Yates et al.[63] Both γδ T cell types undergo auto-activation according to positive feedbacks from their own densities at rate r_{Ti} and have some maximum carrying capacity K_T. γδ T cell replication also receives feedback from blood parasite densities according to another Hill function, where K_{rB} is the density at which the replication rate σ_i is half-max. Each γδ T cell subtype can inhibit the other according to an exponential decay parameter ω_i. Finally, γδ T cells die at rate μ_T.

$$\frac{dT_{17}}{dt} = T_{17}\left(\frac{1}{1+\left(\frac{K_L}{L+1}\right)^{n_L}}\right)\left(r_{T1} + \sigma_1\left(\frac{1}{1+\left(\frac{K_{rB}}{B+1}\right)^{n_B}}\right)\right)\left(\frac{1}{1+\left(\frac{T_{17}}{K_T}\right)^{n_T}}\right) * e^{-\omega_{17} T_N} - \mu_T T_{17} \quad \text{(Equation 3)}$$

$$\frac{dT_N}{dt} = T_N\left(\frac{1}{1+\left(\frac{K_L}{L+1}\right)^{n_L}}\right)\left(r_{T2} + \sigma_2\left(\frac{1}{1+\left(\frac{K_{rB}}{B+1}\right)^{n_B}}\right)\right)\left(\frac{1}{1+\left(\frac{T_N}{K_T}\right)^{n_T}}\right) * e^{-\omega_N T_{17}} - \mu_T T_N \quad \text{(Equation 4)}$$

Sequestration and ECM-associated damage

Sequestration of erythrocytes (S) to the endothelium contributes to the onset of ECM, and occurs at rate γ_B in a blood parasite density-dependent manner. The maximal rate of BS-dependent sequestration is modified by overall γδ T cell density (half-max is represented by K_S). T_N cells aggrevate sequestration at rate γ_N, while T_{17} cells dampen sequestration at rate ε (e.g., through the stimulation of new reticulocytes). Sequestered erythrocytes have a background clearance rate of μ_C. Sequestration-induced damage **(D)**, representing ECM, accumulates at rate β, with K_D representing the sequestration levels that produce half-maximum damage rates. Damage can be repaired by the host at rate μ_D.

$$\frac{dS}{dt} = \gamma_B B\left(\frac{1}{1+\left(\frac{T_{17}+T_N}{K_S}\right)^{n_S}}\right) + \gamma_N T_N - \varepsilon T_{17} - \mu_C S \quad \text{(Equation 5)}$$

$$\frac{dD}{dt} = \beta\left(\frac{1}{1+e^{-aS+K_D}}\right) - \mu_D D \quad \text{(Equation 6)}$$

Parameters and assumptions

All simulations were run using the ode45 solver in MATLAB (R2016a). The model was first parameterized (Extended Data Table S1) to recapitulate empirical parasite and ECM dynamics in the absence of liver stages (e.g. Figure 1B). Then, the model was parameterized to produce differences in empirically-derived γδ T cell proliferation patterns (e.g. Figures 2F and S2E) according to blood stage and liver stage parasite density, respectively. There are some significant asymmetries in these parameters. Most notably, γδ17 T cells proliferate slightly more rapidly than γδIFN T cells in the presence of the liver stage parasites (parameter rt_i), but γδIFN T cells proliferate more rapidly in the presence of blood stage parasites (σ_i), as suggested by our experimental data. γδ T cell proliferation rates and hill coefficients are based on values used in Yates et al.[63] In addition, the model suggests that to achieve the empirically observed mortality effects, γδ T cell-dependent processes override the source of BS-dependent pathology that predominates in the absence of liver stage (i.e. *nS* is high), as might be expected under a scenario where γδ T cells have hierarchical priority in coordinating responses over innate immune responses to blood stage. Currently, to reflect experimental conditions, there is no transition of liver stages to blood stages (tr = 0), but this parameter could be modified in the future to model natural sporozoite infection. The model is reasonably sensitive to hill function coefficients; these are kept constant in the different simulations.

Modelling the influence of transmission frequency on γδ T cell dynamics

While an increase in γδ17 activity may contribute to clinical tolerance of malaria infection in frequently exposed individuals, the mechanisms that regulate this activity are unclear. Previous studies have noted an upregulation of inhibitory checkpoint molecules such as Tim-3 in the Vγ9Vγ2 T cells of frequently exposed individuals.[37] Thus, it is possible that over the long term, frequent exposure leads to exhaustion or depletion of these subsets, or possibly a phenotypic shift away from pro-inflammatory IFN-γ production toward a more NK-cell-like ADCC role, as suggested by the upregulation of CD16 in γδ T cells of frequently exposed children.[36] However, the functional contribution of potential exhaustion mechanisms to clinical immunity, and the rate of decline over exposure frequency, has not been directly tested.

Could the γδ17-dependent active regulation of γδIFN and promotion of tolerance explain the pattern of a reduction in severe malaria with increasing exposure frequency, whether or not γδ T cells actually become exhausted or otherwise dysfunctional? To test this question, we built a discrete time model of γδ T cell boosting and interaction among the IFN-γ- and IL-17-producing subsets. Each time step represents a 2-week period, and we monitored hosts over time for 36 months, similar to timescales in Jagannathan et al.[35,37] and Farrington et al.[36] Hosts could become re-exposed to infection at a frequency of once per year to once per month, roughly reflecting the range of transmission frequency for different human populations (e.g. Farrington et al.[36]). To keep the model as simple as possible, we assume that the associated probability of developing severe malaria is likely to decrease as γδ17 T cell levels increase, and thus we recorded these levels (scaled between 0 and 1) as the primary output from the model. We assume that γδ T cell levels (both IFN-γ- and IL-17-producing, with each subset indexed in *i*) decay over time at rate b_i, with longer periods between infections leading to more cell decay. These decay rates can be symmetrical or asymmetrical among γδ T cell subtypes, although we assume symmetrical (default β = 0.05).

Each infection event can potentially stimulate the proliferation of both subsets of γδ T cells in a sporozoite-density-dependent manner (represented by f(spz), below) as suggested by our mouse data, although we simplify our initial investigations by assuming a constant dose of 200 spz per infection event. To reflect the different hypotheses concerning the waning of functional γδT responses with exposure frequency, we allow for two distinct but not mutually exclusive possibilities:

a) Frequent re-boosting of γδ T cells by exposure events leads to the accumulation of exhaustion markers (coefficient c_i, scaled between 0 and 1) on each cell subtype, and this accumulation (at a magnitude of w_i, with default w = 0.05 per infection event) can be symmetrical or asymmetrical among subtypes, although we assume symmetrical here. The cells can clear these markers at rate k_i, such that more time between infection events allows for revival. We allow cells to be very good at clearing these markers (k_i = 0.04) or struggle to clear them, and remain susceptible to exhaustion (k_i = 0.005). The maximum rate of cell proliferation upon new infection (r_i) is dampened in proportion to the accumulation of exhaustion markers (effective $r = r_i^*(1\text{-}c_i)$). Thus, increasing infection frequency could lead to γδ T cell exhaustion and the inability of these cells to produce inflammation.
b) Each γδ T cell subtype inhibits the proliferation and/or effective function of the other subtype, as first represented in the within-host model, with efficiency y_i. Here, we have simplified this negative inhibition to an exponential decay term as befits the discrete-time dynamics. These negative feedbacks prevent either γδ T subtype from proliferating to maximum levels as long as $y_{IFN} = y_{17}$ and y_i is not a trivial number. At y_i = 1, the subtypes inefficiently inhibit each other, and as y_i increases to 2 or 3 they become more efficient. Here, we assume that y_i is either i) symmetrical among subtypes, or ii) that γδ17 are more efficient at inhibiting the effects of γδIFN than vice versa (y_{IFN} = 2, y_{17} =3), as suggested by the dynamics of the within-host model.

Thus, the dynamics of the system over repeated infection events (*v*) can be represented by Equations 7 and 8, where each subtype *i* increases in a sporozoite-dependent manner unless inhibited by exhaustion (*c*) and/or each other (*y*), and both cell decay (*b*) and the clearance of exhaustion markers (*k*) is dependent on time (t) between exposure events:

$$T_{i(v+1)} = \left(T_{i(v)} - b_i(t)T_{i(v)}\right) + f(spz)(1 - c_i)e^{-yi*Tx} \quad \text{(Equation 7)}$$

$$c_{i(v+1)} = c_{i(v)} + w_i c_{i(v)} - c_{i(v)} k_i(t) \quad \text{(Equation 8)}$$

Default parameter values are presented in Extended Data Table S2. There is little experimental data with which to precisely estimate key values or functional forms of model parameters like Vγ9Vδ2 T cells decay, the relationship between exhaustion marker quantity and proliferation rates, or inhibition dynamics. Moreover, many variables are scaled between 0 and 1 for simplicity and tractability. Therefore, we caution against quantitative clinical interpretations of model results or even interpretation of the precise functional form (e.g. linear, concave) of model predictions, particularly with regard to human data, and instead aim here to compare broad qualitative results in our different scenarios.

QUANTIFICATION AND STATISTICAL ANALYSIS

Statistically significant differences between two different groups were determined using Log-rank (Mantel-Cox) test, non-parametric two-tailed Mann-Whitney test or Unpaired two-tailed t-test, as indicated. All the tests were carried out in GraphPad Prism except for those performed for parasitemia. The up-slopes of the growth of blood stage parasites over the first week, i.e., the period of ECM establishment, (for comparisons of parasitemia) or the down-slopes for loss of reticulocytes (from day 4 to minimum level) were analyzed using linear mixed-effects models. In this approach, we use all the measurements available for each mouse, using mouse ID as the grouping (or random) factor to account for the repeated measurements made in each animal. We tested the effect of the experimental condition (e.g., dose of BS infection) by analyzing the interactions of the slope of growth over time post infection with the experimental condition. We report these differences. Assumptions and appropriateness of the fitted models and the distribution of residuals were checked by visual inspection of fitting and residual plots. The best model for the data was chosen using a log likelihood test, which accounts for different numbers of parameters. For these analyses we used the lme function of the NLME package of R (http://cran.r-project.org/). Biological replicates (n) refers to the number of mice, pooled from experiments performed independently (ind. exp.), as indicated in the figure legends. Sample sizes on mice experiments were chosen on the basis of historical data. No statistical methods were used to predetermine sample size.